Cold-formed steel beam-to-column bolted connections for seismic applications

Ioannis Papargyriou[1*], Seyed Mohammad Mojtabaei[1,2], Iman Hajirasouliha[1], Jurgen Becque[2], Kypros Pilakoutas [1]

[1] Department of Civil and Structural Engineering, The University of Sheffield, Sheffield S1 3JD, UK

[2] Department of Engineering, University of Cambridge, CB2 1PZ, Cambridge, UK

* Corresponding author, E-mail: i.papargyriou@sheffield.ac.uk

Abstract

Cold-formed steel (CFS) portal frames are gaining increased popularity around the world. The structural performance of these frames is to a large extent controlled by the CFS beam-to-column connections, which in most practical applications transfer the loads through the beam web using a gusset plate, while the flanges are left unconnected. This can lead to premature local buckling failure of either the CFS beam web in the connection zone or the gusset plate, leading to poor seismic performance. This paper aims to develop two new connection configurations which engage the flanges in the connection behaviour. In conjunction, practical seismic design recommendations are presented, which allow a balance between the load carrying capacity of the connections and their seismic performance to be reached. Detailed Finite Element connection models, taking into account material nonlinearity and initial geometric imperfections, are developed and validated against experimental data. The validated FE models are then used to conduct a comprehensive parametric study to investigate the effects of key design parameters, including the beam thickness and the gusset plate shape and thickness, on the moment-rotation behaviour of the connections. Based on the results, suitable connections, which balance strength with seismic performance, are introduced. Their seismic performance is evaluated in terms of ductility, energy dissipation and damping coefficient, leading to some practical design recommendations commensurate with different seismic performance levels.

Keywords: Cold-formed steel (CFS); Moment-resisting connections; Flange-connected joints; Optimum design; Performance based design; Ductility

1 Introduction

The demand for cold-formed steel (CFS) systems has significantly increased over the past decade. Among them, CFS portal frames have become a popular structural system, mainly for single-storey industrial buildings. The seismic performance of CFS frames is to a large extent controlled by the beam-to-column connections, which are implemented in a fundamentally different way compared to the traditional frames composed of hot-rolled sections. Consequently, the use of CFS moment-resisting frames in seismic regions is still very limited due to the challenges associated with developing resilient moment-resisting CFS connections that can prevent premature local buckling failure of the thin-walled elements. As a result, strap-braced load-bearing stud walls [1–5] are currently the dominant lateral force-resisting system used in multi-storey CFS structures, while moment-resisting frame systems are generally reserved for low-rise CFS portal frames.

The behaviour and design of CFS Web-Connected (W-C) bolted connections have been previously investigated experimentally and numerically in several research studies. Chung and Lau [6] and Wong and Chung [7] carried out a series of experiments on CFS bolted beam-to-column connections, using various shapes of gusset plates. They demonstrated the practical feasibility of these connections, which achieved a moment resistance ranging between 42% and 84% of the bending moment capacity of the beam and exhibited a semi-rigid response. Similar observations were reported by Lim and Nethercot [8], who tested apex and eaves joints of CFS portal frames to study their behaviour under monotonic bending. The joints failed by cross-sectional instability of the beam, triggered by web buckling. The authors also identified an increased bolt group length and an increased number of bolts as the main factors which can improve the rotational stiffness of the connections. Dubina et al. [9] tested eaves and apex joints of portal frames under monotonic and cyclic loading and observed bearing elongations of the bolt holes, as well as local buckling failure in the beam adjacent to the connection, which led to a low overall ductility. In the same study, full-scale testing of a pair of portal frames with bolted connections revealed that these systems lose their capacity rapidly once local buckling occurs in the connections. In another relevant study, Zhang et al. [10] carried out three full-scale tests of portal frames and concluded that the stiffness of the eaves and apex connections significantly depends on the bolt tightness and the bracket (i.e. gusset plate) dimensions. Blum and Rasmussen [11] also quantified the stiffness of portal frame connections based on the results of a series of experiments, while Bučmys et al. [12] used an approach based on the component method. In another study, Rinchen and Rasmussen [13] established simplified nonlinear moment-rotation relationships for eaves, apex and base connections. More recently, Sabbagh and Torabian [14] conducted a proof-of-concept study on a joist-stud framed design for semi-rigid floor-to-wall connections and proposed a method to estimate the rotational stiffness of such connections.

Several studies have demonstrated the capacity of W-C connections to be considerably affected by the bolt group length [8,15–19]. This effect was initially attributed by Lim et al. [8] to the presence of a bimoment in the connection, and different design approaches were presented using the Direct Strength Method (DSM) and the Direct Design Method (DDM) to account for this bimoment [15–17]. However, more recently, Mojtabaei et al. [18,19] have argued that the influence of the bolt group length in doubly symmetric beam sections can instead be attributed to a shear lag effect, and the researchers subsequently proposed design equations for the connection strength under various load combinations.

The cyclic behaviour of CFS beam-to-column W-C connections was studied experimentally and numerically by Sabbagh et al. [20,21]. It was reported that curved beam flanges and welded-in vertical beam stiffeners delayed local buckling failure and improved the bending moment capacity and ductility by 35% and 75%, respectively. The connections were categorised as 'Rigid', based on their rotational stiffness determined according to Eurocode 3 [22]. A similar experimental study was conducted by Serror et al. [23]. However, in this case, the column consisted of a hot-rolled profile. It was reported that the presence of stiffeners in the beam improved the connection characteristics, while additional flange bends averted premature buckling of the flanges but could not prevent buckling of the web.

Shahini et al. [24] numerically and experimentally investigated the effect of different bolt arrangements on cyclic connection behaviour, and demonstrated that a circular arrangement with slotted holes in the gusset plate can delay local buckling failure in the CFS beam and consequently improve the cyclic response. In a similar study, Ye [25] developed detailed Finite Element (FE) models of CFS moment-resisting connections while taking into account material nonlinearity and geometric imperfections and studied the effects of key design parameters, such as the cross-sectional shape of the beam and the bolt arrangement, on the cyclic performance. In a follow-up study by Ye et al. [26], the seismic characteristics of beam-to-column connections which mobilise a friction-slip fuse mechanism were assessed and compared with similar connections where bolt slippage is prevented. However, no experimental verification of the feasibility of prestressing CFS connections was provided as part of this study. Mojtabaei et al. [27] improved the seismic performance of bolted moment connections in terms of ductility and energy dissipation by using optimised CFS beams with enhanced non-linear post-buckling behaviour.

Currently, CFS moment-resisting connections are mostly implemented as W-C connections. This has the implication that, unlike in moment-resisting connections in hot-rolled steel structures, the beam and column flanges do not directly participate in transferring the applied loads. This considerably affects the stiffness, load bearing capacity and resilience of these connections, especially under extreme loading events such as earthquakes and blast. Virtually no research exists which explores alternative CFS moment-resisting connection geometries, in particular with respect to the effects of connecting the flanges in various ways to obtain stiffer connections with higher moment capacities. More generally, there is still insufficient knowledge about the behaviour of CFS moment-resisting connections (especially in seismic areas) and this results in low confidence among designers and fabricators, hampering the further evolution and implementation of CFS structures. More research is needed regarding the structural performance parameters of CFS connections, particularly focusing on their deformability, ductility, and energy dissipation capacity.

The present work aims to address these important issues by developing and studying two new configurations of beam-to-column bolted connections: Flange-Connected (F-C) and Web-and-Flange-Connected (WF-C) joints, which benefit from the load transfer contribution of the flanges. The performance of the newly proposed connections is compared to that of the conventional Web-Connected (W-C) connections (see Table 4). To achieve this, detailed ABAQUS [28] FE models were employed, which were first validated against experimental results. A parametric study further investigated the effect of key design parameters, such as the beam thickness and the gusset plate shape and thickness, on the moment-rotation behaviour of each type of connection. The connections with the overall best performance, considering both capacity and rotational behaviour, were identified and compared in terms of ductility, energy dissipation and damping coefficient, leading to practical seismic design guidance linked to different seismic performance levels.

2 Description of the ABAQUS numerical models

Sabbagh et al. [20] previously carried out a comprehensive experimental programme on W-C connections, where the webs of back-to-back channel beam and column sections were bolted to a gusset plate. The web panel zone was stiffened to prevent local failure in the column, in alignment with the commonly accepted strong-column/weak-beam philosophy in earthquake engineering. More detailed information about these experiments can be found in [29]. In this section, the results of two of these tests, pertaining to specimens A1 and B1, which were tested under cyclic loading conditions, were selected to validate the numerical models. The models were developed using the ABAQUS software [28] and accounted for material nonlinearity and initial geometric imperfections. Various previous studies have demonstrated that the adopted modelling approach, described below, can be used to simulate the nonlinear behaviour of CFS systems in an effective and reliable way [17,21,26,30,31].

2.1 Material properties

The nonlinear stress-strain relationships of the CFS beam and the gusset plate materials were incorporated in ABAQUS [28] utilizing a two-stage material model proposed by Heidarali and Nethercot [32], fitted to the results of coupon tests reported by Sabbagh et al. [29]. In a first stage, the stress-strain behaviour was defined up to the 0.2% proof stress ($\sigma_{0.2}$) using Eq. (1), initially proposed by Ramberg and Osgood [33] and later modified by Hill [34]. A straight line with a slope $E = \frac{E_0}{100}$ was used in the second stage, as expressed by Eq. (2). In Eqs. (1) and (2), $\varepsilon_{0.2}$ is the strain corresponding to the $\sigma_{0.2}$ proof stress, E_o stands for the elastic modulus (which was taken as 210 GPa), and n is a constant which was assumed equal to 10, as recommended by Rasmussen [35].

$$\varepsilon = \frac{\sigma}{E_o} + 0.002\left(\frac{\sigma}{\sigma_{0.2}}\right)^n, \qquad \sigma \leq \sigma_{0.2} \tag{1}$$

$$\varepsilon = \varepsilon_{0.2} + \frac{\sigma - \sigma_{0.2}}{E}, \qquad \sigma \geq \sigma_{0.2} \tag{2}$$

In a next step the engineering strains and stresses were converted to logarithmic plastic strains and stresses, while the linear kinematic hardening rule available in ABAQUS was adopted to simulate the hardening behaviour of the material. The (engineering) material properties of the connection components are summarised in Table 1 for reference tests A1 and B1.

2.2 Finite element type and mesh size

The S4R general-purpose finite element available in ABAQUS was employed to model all connection components, since it has previously proven to be accurate in capturing the behaviour of CFS elements and connections [18,19,31,36,37]. This four-noded shell element has six degrees of freedom per node. It can account for nonlinear material properties and finite membrane strains, and features hourglass control and reduced integration. Following a mesh sensitivity analysis, a mesh size of 10×10 mm was selected to guarantee adequate numerical accuracy while keeping the computational time within acceptable limits.

2.3 Bolt modelling

The bolt behaviour was simulated by employing the Discrete Fastener feature of the ABAQUS software [28]. This modelling technique creates attachment lines between the fastening points located on the connecting surfaces, as shown in Fig. 1(a-b). An influence radius was assigned to each fastening point, with the implication that the displacements of the fastening points are coupled to the average displacements of the nodes within this radius. An influence radius equal to 8 mm was used in the FE models, corresponding to half the bolt diameter, as recommended in [18,31]. In this study, rigid bearing behaviour was assumed for the bolts connecting the column to the gusset plate, while combined friction and bearing behaviour was modelled for the beam to gusset plate bolts. This was motivated by the fact that bolt hole elongation is typically more critical in the beam due to its lower thickness compared to the column and the gusset plate. In the A1 and B1 tests, preloading forces of P_b=88 kN and P_b=70 kN, respectively, were applied to the head of the bolt by using a torque wrench, which generated friction between the beam web and gusset plate. When friction is overcome, bearing action of the bolts is mobilised, which was modelled using the equations proposed by Fisher [38]:

$$R_B = R_{ult}[1 - e^{-\mu\left(\frac{\delta_{br}}{25.4}\right)}]^{\lambda} \tag{3}$$

$$R_{ult} = 2.1 d t F_u \tag{4}$$

where R_B is the bearing force, R_{ult} is the ultimate bearing strength, δ_{br} is the bearing deformation (in mm), t is the plate thickness, d is the bolt diameter, F_u is the ultimate tensile strength of the plate material, and μ and λ are constants equal to 5 and 0.55, respectively, according to the recommendations by Uang et al. [39]. The load-displacement behaviour of the bolts obtained from the above-mentioned equations is shown in Fig. 2 for tests A1 and B1. It should be noted that in experiments A1 and B1 [29], no bolt shear failure was observed.

2.4 Boundary conditions and interactions

The boundary conditions imposed onto the FE models of the W-C connections are shown in Fig. 3. All three translational degrees of freedom of the nodes at the bottom of the column were restrained (U_X=U_Y=U_Z=0), while the horizontal displacements of the top nodes were also restrained (U_X=U_Y=0). The out-of-plane deformations of the beam were prevented at the locations where the lateral bracing system was positioned in the experiments (see Fig. 3). The webs of the back-to-back channels were connected at three different locations using “Tie” constraints to simulate the bolts outside the connection zone. Additionally, tie constraints were used to connect the column stiffeners rigidly to the column web and flanges. The “Hard” contact feature was employed between the connecting faces of the beam webs and the gusset plate to avoid penetration of the surfaces into each other. All degrees of freedom of the beam end section, where the external load was applied, were coupled to a Reference Point (RP) located at mid-height of the webs.

2.5 Initial geometric imperfections

In the experiments, as well as in the FE model, the global buckling mode of the CFS beam was prevented due to the presence of the lateral bracing system. Hence, only a local or a distortional imperfection (whichever mode had the lower critical buckling load) was included in the FE models. Imperfection amplitudes of $0.94t$ and $0.34t$ (where t is the plate thickness) were used for the distortional and local imperfections, respectively, as recommended by Schafer and Peköz [40]. These are the 50% values of the cumulative distribution function of experimentally measured imperfections and represent 'most probable' values. Since these amplitudes are only applicable for $t \leq 3$ mm, Walker's [41] equation was instead used for plate thicknesses larger than 3 mm:

$$w_d = 0.3t\,\lambda \tag{5}$$

where w_d is the imperfection amplitude and λ represents the cross-sectional slenderness, which is calculated as:

$$\lambda = \sqrt{\frac{M_y}{M_{cr}}} \tag{6}$$

In the above equation, M_y is the yield moment of the cross-section and M_{cr} is the elastic local/distortional buckling moment, which was obtained using the CUFSM software [42]. To generate the overall shape of the geometric imperfections, an elastic eigenvalue buckling analysis was performed in ABAQUS. The shape of the critical buckling mode was then scaled by the appropriate imperfection amplitude.

It should be noted that previous research on CFS portal frame connections failing by local buckling [18] has demonstrated through sensitivity studies that the connection capacity is only affected to a very minor extent by imperfections. This is somewhat expected, since the local mode has a stable post-buckling range, and no interaction with other modes takes place in the problem under consideration [43].

2.6 Loading

The FE models of the connections were loaded in a displacement controlled manner under both monotonic and cyclic conditions. While a maximum displacement of 200 mm was applied for monotonic loading, in the cyclic analyses the loading protocol presented in section S6.2 of the AISC 341-16 [44] provisions (as used in the corresponding experiments) was adopted. This protocol includes the following steps (Fig. 4):

(1) 6 cycles at $\theta = 0.00375$ rad

(2) 6 cycles at $\theta = 0.00500$ rad

(3) 6 cycles at $\theta = 0.00750$ rad

(4) 4 cycles at $\theta = 0.010$ rad

(5) 2 cycles at $\theta = 0.015$ rad

(6) 2 cycles at $\theta = 0.02$ rad

(7) 2 cycles at $\theta = 0.03$ rad

(8) 2 cycles at $\theta = 0.04$ rad

(9) Continue loading in increments of $\theta = 0.01$ rad, applying two cycles of loading in each step.

2.7 Numerical model validation

'Static General' analyses were carried out using the High-Performance Computing (HPC) facilities at the University of Sheffield.

Fig. 5 compares the moment-rotation relationships extracted from experiments A1 and B1 with the corresponding FE predictions for both cyclic and monotonic loading conditions. The bending moments were made dimensionless relative to the plastic moment of the CFS beam (M_p) and the rotation of the connection was determined as the ratio of the beam tip displacement to the length of the beam up to the gusset plate.

Fig. 5 indicates that the FE models were able to simulate the behaviour of both tested connections with good accuracy over the whole loading range. The initial stiffnesses of the tested connections were virtually identical to those obtained from the FE models, while the experimental and predicted flexural capacities compared as 54.3 kNm and 51.6 kNm for test A1, and 81.7 kNm and 82.4 kNm for test B1. A comparison between the FE cyclic and monotonic results also indicated that the initial stiffness and the connection capacities were coincident in both cases. However, the results of the monotonic analyses slightly underestimated the cyclic stiffness degradation rate. Failure of the connections under both monotonic and cyclic loading was predicted by the FE analyses to be initiated by local buckling of the beam web, followed by buckling of the compression flange, consistent with the experiment, as shown in Fig. 6. These observations confirm the adequacy of the adopted FE models in this study. It should be noted that these modelling techniques have also been verified against experiments reported by Lim and Nethercot [8] in two recent publications by the authors [18,19].

3 Development of new connection configurations

This section discusses the development of two new configurations of bolted CFS beam-to-column connections, which are capable of transferring the applied loads through either the flanges only (F-C connection) or both the flanges and the webs (WF-C connection). The behaviour and failure mechanism of these connections, alongside W-C connections of the type introduced in Section 2, were investigated under monotonic loading conditions while considering various beam thicknesses and gusset plate shapes and thicknesses. The obtained moment-rotation curves were compared in terms of their relevant performance criteria, including the bending moment capacity, the ultimate rotation and the rotational rigidity in relation to code-prescribed categories. As shown in the previous section, the monotonic loading results can be considered representative of both monotonic and cyclic loading when considering these parameters. The connections displaying the best performance were identified for each connection configuration (W-C, F-C and WF-C) and were further investigated under cyclic loading.

3.1 Connection configurations

The proposed W-C connections are assembled by bolting a gusset plate in between the webs of the beam and the webs of the column. The choice of the gusset plate shape is a rather challenging issue encountered in practice since it may cause either architectural limitations or reductions in structural performance. Therefore, as shown in Table 2, three different gusset plate shapes were selected in this study, including a T-shaped plate with sharp corners (further referred to as the 'T-shape'), a T-shaped plate with rounded corners (the 'rounded T-shape') and the rectangular plate with chamfered corners which was employed in the experiment (see Section 2), which is simply referred to as the 'Chamfered shape'. The transition radius of the rounded T-shape was chosen as 350 mm in this study. In Table 4, 3D graphical representations of the different joint configurations are presented.

For the F-C connection configuration, either 'unstiffened' or 'stiffened' top and seat angles were used, bolted to the column and beam flanges, as shown in Table 2. The stiffened angles contained an infill plate to form a haunch. The WF-C connections, on the other hand, were conceived as a combination of the other two configurations, where both a T-shaped gusset plate and unstiffened top and seat angles were used. The bolt group length (l_b) in the CFS beam was consistently taken equal to the beam depth (h), and a fixed number of bolts was used in each type of connection, as illustrated in Table 2. However, the thicknesses of the CFS beam and the gusset plate were varied to investigate their effects and identify the slenderness limits where failure shifted from the gusset plate to the beam. The CFS beam was assigned thicknesses t_b = 1, 2, 4 and 6 mm, whereas the gusset plate thickness was taken as a multiple of the beam thickness (see Table 2). It is thereby noted that for the chosen beam dimensions t_b = 1, 2, 4 and

6 mm correspond to Class 4, 3, 2 and 1 cross-sections according to EC3 [45], respectively. The critical local and distortional buckling stresses for each thickness are listed in Table 3.

The other design parameters were kept constant across all connection models, including the material properties, the locations of the lateral bracing, the lengths of the members, the cross-sectional dimensions and the thickness of the column and its stiffeners (Fig. 7). The 2000 mm long beam and 900 mm long column segments used in the FE models consisted of back-to-back lipped channel and plain channel sections, respectively, with the dimensions (along the centrelines) given in Fig. 7. The modelled beam segment can be considered representative of the part of a beam in a moment-resisting frame between the point of contraflexure and the column. The material properties listed in Table 1 were used for all FE models. Lateral bracing was provided along the length of the beam at 500 mm spacing.

3.2 Evaluation of connections under monotonic loading

3.2.1 Performance criteria

The rotational behaviour of the connections was quantified through various performance parameters related to their (i) rotational rigidity, and (ii) rotational capacity. The latter was assessed in two distinct ways, as detailed below.

To assess the rigidity of the connections, the provisions of EN 1993-1-8 [22] were followed, in which the moment-rotation relationship of a connection is derived by calculating the bending moment (M_j) at the face of the column and by taking the corresponding rotation (ϕ) as the difference between rotations (ϕ_1) and (ϕ_2), shown in Fig. 8(a). The initial stiffness ($S_{j,ini}$) is then defined as the secant slope of the moment-rotation curve (see Fig. 8b) at a value of $2/3\times M_{j,R}$, where ($M_{j,R}$) is the moment resistance of the connection. Subsequently, the connection is categorised as either Rigid, Semi-Rigid or Pinned, by comparing the initial stiffness ($S_{j,ini}$) with the limits shown in Fig. 8(c). A Rigid (R) connection has an initial stiffness greater or equal to

$k_b \times E \times I_b/L_b$, where k_b=25 for an unbraced system, (E) is the elastic modulus, (I_b) is the second moment of area of the beam and (L_b) is the beam span, measured between the centre lines of the columns. The connection is classified as Pinned (P) if the initial stiffness is smaller or equal to 0.5× $E \times I_b/L_b$. For intermediate values, the connection is Semi-Rigid (S-R).

A first performance parameter adopted to assess the rotational capacity of the connections consisted of the ultimate rotation, taken equal to the minimum of 0.06 rad and the rotation corresponding to a 20% drop in moment from the peak point in the moment-rotation curve. This is based on the recommendations given by the American Seismic codes: AISC 341-16 [44] and FEMA-350 [46].

A second indicator of inelastic rotational capacity is provided by the American Seismic Provisions for Structural Steel Buildings (AISC 341-16), in which moment-resisting frames are classified into three categories: Ordinary Moment Frames (OMF), Intermediate Moment Frames (IMF) and Special Moment Frames (SMF). The connections of SMFs and IMFs should be able to accommodate minimum storey drift angles of 0.04 rad and 0.02 rad, respectively, while OMFs do not meet the 0.02 rad value. It should be noted that using OMFs in seismic regions is prohibited by most seismic design codes.

3.2.2 Moment-rotation results and discussions

3.2.2.1 W-C connections

Fig. 9 shows the moment-rotation curves obtained for the W-C connections (see Table 2) with various beam thicknesses (t_b), gusset plate thicknesses (t_g) and gusset plate shapes (①: T-shape, ②: rounded T-shape and ③: chamfered shape) up to their ultimate rotations. Both the moment and the rotation in Fig. 9 were calculated based on the location of failure, which was idealised to coincide with the end of the gusset plate, i.e. at a distance of 1700 mm from the cantilever tip (Fig. 7). Failure occurred by either local buckling of the beam immediately adjacent to the connection (followed by distortional buckling past the peak load), or local buckling of the gusset plate.

It is seen that the connections with the chamfered gusset plate (i.e. ③) reached higher moment capacities (M_{max}) than their 'rounded T-shape' counterparts (i.e. ②) for gusset plate thicknesses t_g with $t_b \leq t_g \leq 1.5t_b$, while both configurations reached the same moment capacities for gusset plate thicknesses with $2t_b \leq t_g \leq 3t_b$. The latter is due to gusset plate failure no longer being critical. This makes the rounded T-shape a suitable alternative to the conventional chamfered gusset plates for those higher thicknesses. The T-shaped gusset plate connections exhibited the lowest moment capacity among the three selected gusset plate shapes, which can be attributed to the abrupt change in depth of the gusset plate at the column face, leading to stress concentrations and premature buckling at the corners, especially for lower plate thicknesses.

Table 5 lists the dominant failure modes for all connections, which consisted of either local buckling of the CFS beam (B) or local buckling of the gusset plate (GP). Fig. 10 shows examples of the typical failure modes of the connections with T-shaped, rounded T-shaped and chamfered gusset plates for t_b=4 mm and t_g=1.5t_b, where the yielding areas are highlighted in grey. It is seen that significant plasticity developed in the beam for the connection with the chamfered gusset plate, while the connections with T-shaped and rounded T-shaped gusset plates mainly experienced plasticity in the gusset plate rather than the beam.

All connections with T-shaped gusset plates were classified as Semi-Rigid (S-R) according to EC3 [22] (Table 5). All rounded T-shaped connections also performed as Semi-Rigid joints, with the exception of those with the thickest gusset plates connecting Class 3 or 4 beams, which were classified as Rigid (R). With the chamfered connections, however, mostly Rigid (R) connections were obtained in Class 2, 3 and 4 beams, with the exception of those with the thinnest gusset plates ($t_g = t_b$ for Class 2-4, and $t_g = 1.5t_b$ for Class 2), which were Semi-Rigid.

The ultimate rotation and the corresponding classification according to AISC 341 [44] (see section 3.2.1) are also listed in Table 5. All studied connections with Class 1 beams were categorised as Special Moment Frame (SMF) connections. The same category was obtained for the connections with Class 2 beams, except for the case where t_b=t_g. On the contrary, none of the connections with Class 3 or 4 beams performed as SMFs, which indicated that they are not suitable for regions with high seismicity.

3.2.2.2 F-C connections

The F-C connections considered in this study employed either stiffened or unstiffened angle sections, instead of a gusset plate, to transfer shear and bending moments to the column (see Table 2). The thicknesses of the angle sections were taken as multiples of the beam thickness, and ranged between t_b and $6t_b$ for the 1 mm and 2 mm thick beams, and between t_b and $3t_b$ for the 4 mm and 6 mm thick beams (as to not exceed a maximum value of 18 mm). In the case of stiffened angles, the thickness of the stiffening plate was taken equal to the thickness of the angles. Fig. 11 presents the moment-rotation relationships, up to the ultimate rotation, for beam thicknesses of 1, 2, 4 and 6 mm, where ① and ② stand for connections with unstiffened and stiffened angles, respectively. It was observed that using stiffened angles increased both the flexural stiffness and the capacity of the connections by an average factor of 4, compared to the connections with unstiffened angles. This increase was especially evident for the connections with Class 3 and 4 beam sections (i.e. 1 mm and 2 mm thickness). Table 6 presents the failure modes of the studied F-C connections. The unstiffened angles failed due to yielding under combined bending and tension/compression, while the connections employing stiffened angles failed due to either local buckling of the stiffening plates and angle plastification (indicated with 'A' in Table 4), or local/distortional buckling of the beam (indicated with 'B'). For small angle thicknesses the F-C connections with Class 2, 3 and 4 beam sections (i.e. 1, 2 and 4 mm thickness) practically acted as pin connections, and are hence unsuited for seismic use in unbraced moment-resisting frames. Conversely, the studied connections with Class 1 beam sections (i.e. t_b=6 mm) were determined to all be Semi-Rigid. Incorporating stiffened angles, as opposed to unstiffened angles, improved the rigidity of the connections from Pinned to Semi-Rigid in many cases, as shown in Table 6.

Due to the deformability of the unstiffened angles under combined tension/compression and bending, with a gap opening up between the beam and the column on the tension side, all connections with unstiffened angles reached an ultimate rotation of at least 0.06 rad without a significant drop in moment resistance and satisfied SMF requirements according to the AISC 341 [44] classification. During these large rotations the beam remained unbuckled (see Fig. 12(a)). On the other hand, stiffening the top and seat angles with infill plates dramatically reduced their deformations, and as a result, failure shifted to the beam element instead (see Fig. 12(b)). In this case, the deformations and yielding on the compression side of the beam are mostly concentrated around the local buckle, with the top infill plate attracting little stress.

This has the potential to reduce the rotational capacity to below 0.06 rad and alter the connection behaviour from a SMF to an IMF for the larger plate thicknesses and Class 3 and 4 beam sections. These results indicate that for seismic applications, using very thick stiffened angle sections to connect thin-walled beam sections may not be appropriate.

3.2.2.3 WF-C connections

The WF-C connections consisted of a T-shaped gusset plate in combination with unstiffened top and seat angles, connecting both the web and the flanges of the beam (see Table 2). The moment-rotation relationships of the studied WF-C connections, up to their ultimate rotations, are shown in Fig. 13 for different beam thicknesses (i.e. t_b=1, 2, 4 and 6 mm) and gusset plate thicknesses (t_g=t_b, 1.5t_b, 2t_b, and 3t_b). The thickness of the angles was also taken equal to t_g. As expected, increasing the gusset plate and angle thicknesses generally increased both the flexural capacity and the rotational stiffness of the WF-C connections. As illustrated in Fig. 14 (and listed in Table 7), the failure mode of the WF-C connections was identified to be local/distortional buckling of the CFS beam for the connections with the thickest gusset plate and angles (i.e. t_g=3t_b), while in the other cases the failure mode was yielding of the gusset plate and/or the angles. This is reflected in the rotational capacities (ϕ_{max}) of the connections listed in Table 7: increasing the gusset plate and angle thickness up to t_g=2t_b enhanced the rotational capacity, while for higher plate and angle thicknesses the rotational capacity decreased due to distortional buckling of the CFS beam.

Based on the AISC [44] classification, all connections with Class 1 beam sections were categorised as SMFs. Connections using Class 2 and 3 beams also satisfied the SMF requirement when the gusset plate thickness $t_g \leq 2t_b$. On the contrary, WF-C connections with Class 4 beam sections always belonged to IMFs or OMFs, which indicates they are not suitable for regions with high seismicity. In terms of rotational rigidity, all connections needed to be classified as Semi-Rigid according to EC3 [22].

3.3 Selection of most suitable connection configurations for seismic applications

The results regarding the bending moment capacity, ultimate rotation, rotational rigidity and seismic classification of the connections obtained in the previous section were used to identify the connection configurations with the best overall performance for each connection type.

For comparative purposes, the flexural capacity of each connection was normalised with respect to the cross-sectional bending capacity of the beam $M_{u,b}$, obtained from the FE analysis of a beam segment subject to pure bending. This FE model is shown in Fig. 15. The beam remained laterally restrained at discrete locations (i.e. every 500 mm) to prevent global buckling. The length of the beam segment was taken as three times the distortional buckle halfwave length, calculated using the CUFSM [42] software, as suggested by Shifferaw and Schafer [47]. The values of $M_{u,b}$ obtained for the studied cross-sections with thicknesses of 1 mm, 2 mm, 4 mm and 6 mm were calculated to be 10.6 kNm, 32.3 kNm, 79.3 kNm and 121.6 kNm, respectively.

Fig. 16, Fig. 17 and Fig. 18 show the variation of $M_{max}/M_{u,b}$ (where M_{max} is the connection capacity) for various gusset plate and beam thicknesses for the W-C, F-C and WF-C connections, respectively. These figures, along with the results presented in Tables 3, 4 and 5, were used to draw the following conclusions:

- Among the three gusset plate configurations considered for the W-C connections, the rounded T-shape and the chamfered shape are generally preferred over the plain T-shape, because of their higher flexural capacity, higher stiffness and more ductile behaviour (the latter evaluated based on the AISC 341 code). There was no significant difference between the performance of the connections with the rounded T-shape and the chamfered shape in terms of the rotational capacity, stiffness and strength for $t_g \geqslant 2t_b$. However, the rounded T-shape provides more flexibility for the installation of the floor system. Therefore, a rounded T-shaped gusset plate with a minimum thickness of $t_g=2t_b$ was taken forward as the preferred W-C option.
- With regard to the F-C connections, the connections with stiffened angles were demonstrated to be more suitable for seismic applications than those with unstiffened angles, due to their higher flexural capacities (see Fig. 17) and stiffnesses (see Table 6). For the connections with Class 3 and 4 beam sections, the most efficient thickness of the angles and stiffening plates was identified to be $4t_b$. F-C connections with this thickness act as Semi-Rigid and satisfy SMF requirements, while developing around 80% of the beam strength. For the F-C connections with Class 2 beam sections, a thickness of $2t_b$ was preferred for the stiffened angles, as this satisfied SMF requirements while providing

virtually the same rotational capacity and rigidity as the connections with thicker angles. For the F-C connection with Class 1 beams, although using a plate thickness of $3t_b$ resulted in a bending capacity which was about 10% higher than for a thickness of $2t_b$, it may not be practical to use, for instance, 18 mm angles. Therefore, $t_g=2t_b$ was chosen for Class 1 beam sections.

- For WF-C connections, a thickness $t_g=2t_b$ was chosen for the gusset plate and the angles. These connections were able to develop more than 90% of the flexural capacity of the beam section, while maintaining a high rotational capacity and ductile behaviour according to the AISC 341 code (see Table 7).

Table 8 summarises the connections which were selected based on their performance with respect to the criteria in section 3.2.1. It should be noted that the dominant failure mode for the W-C and F-C connections was generally local/distortional buckling in the beam, whereas the WC-F connections exhibited yielding in the gusset plates. While it is possible to prevent yielding of the gusset plate in WF-C connections by increasing its thickness, this would reduce the ultimate rotation capacity and hence the ductility of this connection type.

4 Seismic evaluation of connections with balanced performance

Fig. 19, Fig. 20 and Fig. 21 present the hysteretic moment-rotation relationships of the W-C, F-C and WF-C connections with 'balanced' seismic performance listed in Table 8, including beams of all four cross-sectional classes (i.e. t_b=1, 2, 4 and 6 mm). The results were obtained by applying the cyclic loading protocol shown in Fig. 4 to the FE models. For comparative purposes, the cyclic moment-rotation backbone curve is also presented, which was obtained by plotting the locus of the peak moment points in the first cycle of each loading amplitude.

For the W-C connections with Class 3 and 4 beams, the hysteretic curves exhibited an abrupt strength degradation immediately after reaching the maximum bending moment. For beams with a larger thickness (i.e. Class 1 and 2 sections), on the other hand, the connections experienced a more prolonged amount of plastic rotation before degradation commenced.

F-C connections with Class 2-4 beams comprised a softening branch in their hysteretic behaviour before reaching the ultimate rotation, which was again taken as the minimum of 0.06 rad and the rotation at which a 20% drop from the peak moment was recorded (see Fig. 20(a), (b) and (c)). However, no strength degradation was observed in the hysteretic behaviour of the F-C connection with a Class 1 beam before the ultimate rotation, as shown in Fig. 20(d). This is attributed to the considerably lower slenderness of both the beam and the stiffened angle elements in this case, reducing their susceptibility to local buckling.

The moment-rotation curves of the WF-C connections indicated that, in general, the connection responses were characterised by plastic strain hardening without any strength degradation. This was due to the opening and closing behaviour of the angles, which acted as a seismic fuse and increased the rotational capacity of the connection, postponing connection failure to larger rotations. However, an exception can be seen for the connection with a Class 4 beam. This is attributed to the high slenderness of both the beam and the gusset plate, leading to premature local buckling.

4.1 Ductility

Ductility is an indicator of the ability to sustain plastic deformations without experiencing a significant drop in strength. The ductility of a structure (μ_ϕ) is commonly expressed as the ratio ϕ_u/ϕ_y, where (ϕ_u) is the ultimate rotation and (ϕ_y) is the rotation at yield. In this study, the rotation at yield (ϕ_y) was calculated based on the equivalent energy elastic-plastic method (EEEP) recommended by ASTM E2126 [48]. An iterative procedure was carried out to define the equivalent bilinear elasto-plastic curve so that the net area enclosed between the equivalent curve and the backbone curve was zero (with the area below the backbone curve being taken as negative). As shown in Fig. 22, the rotation at yield (ϕ_y) corresponds to the rotation where a secant line intersecting the backbone curve at 40% of the peak moment (M_{max}) meets a horizontal line extending to the ultimate rotation. The ultimate rotation (ϕ_u) was previously defined in section 3.2.1.

Fig. 23 and Fig. 24 compare the ductility (μ_ϕ) and the yield rotation (ϕ_y) of the connection configurations previously studied in Fig. 19 - Fig. 21. The results indicate that using Class 1 and 2 beam sections generally led to similar ductility level across all connection configurations. However, ductility results varied significantly when Class 3 and 4 beam sections were used, with the F-C and WF-C connections providing significantly higher ductility (by up to 136%) than the W-C joints.

In general, the results presented in Fig. 24 indicate that the equivalent yield rotation depends more on the beam classification than on the connection type. While increasing the thickness of the beam section always led to a higher yield rotation of the connection (see Fig. 24), no such trend could be observed for the ductility.

4.2 Energy dissipation

In this study the area below the idealised EEEP curve up to the ultimate rotation (see Section 4.1) was used to calculate the energy dissipation capacity (E_d) of the various connections conforming to Table 8, and the results are compared in Fig. 25. As expected, the connections with Class 1 and 2 beam sections dissipated significantly more energy than those with Class 3 or 4 beam sections.

All connection configurations with Class 1 beam sections performed similarly in terms of their energy dissipation capacity, as did those with Class 2 beams. On the other hand, F-C and WF-C connections with Class 3 and 4 beam sections provided energy dissipation capacities which were up to 181% and 196% higher, respectively, than those of the corresponding W-C connections.

4.3 Damping coefficient

The equivalent viscous damping coefficient (ξ_{eq}) is another indicator of the energy dissipation capacity of a system, quantifying the energy loss per cycle. As shown in Fig. 26, ξ_{eq} is defined by relating the energy dissipated in the hysteresis loop (E_h) of a particular cycle to the fictitious energy ($E_{(OAB)}+E_{(OCD)}$) dissipated in viscous damping during the same cycle [49], and is calculated using the following equation [30,50]:

$$\xi_{eq} = \frac{1}{2\pi} \cdot \frac{E_h}{E_{(OAB)} + E_{(OCD)}} \tag{7}$$

The points A and C in Fig. 26 correspond to the maximum positive and negative bending moments, respectively. The above quantity was calculated for two different cycles, corresponding to the maximum bending moment (M_{max}) and the bending moment at the ultimate rotation (M_u).

In general, W-C connections were capable of more substantial damping at the ultimate rotation compared to the other connection configurations. This can be attributed to the fact that more material plasticity is developed in W-C connections compared to other types, which in turn increases the plumpness of the hysteresis loop and consequently the value of the damping coefficient.

By comparing the values of the damping coefficients in Fig. 27 and Fig. 28, it can be concluded that in the connections with Class 2, 3 and 4 beams the majority of the cyclic energy was dissipated after the connections reached their maximum bending moment. On the other hand, for the connections with Class 1 beams there was negligible difference between the values of ξ_{eq} at the peak moment and at the moment corresponding to the ultimate rotation, as plasticity was already significantly developed before the attainment of the maximum bending moment. It should also be noted that the WF-C connections with Class 1 and 2 beams reached their maximum bending moment at the ultimate rotation (ϕ_u=0.06 rad), and thus the damping coefficients for both cycles were identical.

5 Conclusions

This study aimed to develop novel CFS beam-to-column bolted connections for seismic applications and evaluate their performance based on a number of established seismic performance criteria.

Detailed FE models of a range of CFS beam-to-column joints were developed, which were first validated against previous experimental data, and accounted for material nonlinearity and initial geometric imperfections. The structural performance of different configurations of Web-Connected (W-C), Flange-Connected (F-C) and Web-and-Flange-Connected (WF-C) joints was assessed while parametrically varying the thicknesses of key components and the shape of gusset plates. Based on the overall performance in terms of flexural capacity, ultimate rotation and rotational rigidity, the most suitable connection configurations for seismic applications were identified. Subsequently, these connections were evaluated under cyclic loading against key seismic performance parameters, including ductility, energy dissipation capacity and damping coefficient. Based on the results of this study, the following conclusions were drawn:

- Among the Web-Connected (W-C) joints, a rounded T-shaped gusset plate with a thickness larger than $2t_b$ was identified as the preferred option across all beam classes. This connection delivers an advantageous combination of bending moment capacity, rotation capacity and stiffness, while the shape of the gusset plate creates a minimal obtrusion when installing the floor system.
- Flange-Connected (F-C) joints employing stiffened top and seat angles exhibited a flexural capacity and rotational stiffness which were on average 4 times higher than those of their unstiffened counterparts. However, the results also indicated that using thick stiffened angle

sections alongside thin-walled beam sections led to a lower rotation capacity. The preferred angle and stiffener thicknesses were $2t_b$ for Class 1 beams, $3t_b$ for Class 2 beams, and $4t_b$ for Class 3 and 4 beams.

- A study of Web-and-Flange-Connected (WF-C) joints, employing both unstiffened top and seat angles and a gusset plate, revealed that plate thicknesses larger than $2t_b$ offered the best combination of flexural capacity, rotational stiffness and rotation capacity across all beam classes.
- Cyclic analyses of the recommended W-C, F-C and WF-C connections indicated that they were all suitable for practical seismic applications, as they provided an acceptable level of ductility while developing more than 80% of the flexural capacity of the connected beam.
- Very similar ductility levels were encountered for Class 1 and 2 beam sections across all connection configurations. However, for Class 3 and 4 beam sections WF-C and F-C connections exhibited up to 136% more ductility than W-C joints.
- In terms of dissipated energy, a similar performance was observed among all connections with Class 1 beams. This was also the case for Class 2 beams. However, for Class 3 and 4 beams the WF-C and F-C connections significantly outperformed the W-C connections by up to two orders of magnitude. On the other hand, W-C connections displayed higher equivalent viscous damping coefficients at the ultimate rotation, reflecting the more extensive development of material plasticity in their components compared to the other types considered.

6 References

[1] K. Velchev, Inelastic Performance of Screw Connected CFS Strap Braced Walls Research Report RP08-5, 2008. https://scholarsmine.mst.edu/ccfss-aisi-spec/88.

[2] L.A. Fülöp, D. Dubina, Performance of wall-stud cold-formed shear panels under

monotonic and cyclic loading Part II: Numerical modelling and performance analysis, Thin-Walled Struct. 42 (2004) 321–338. doi:10.1016/S0263-8231(03)00063-6.

[3] J.. Leng, B.W.. Schafer, S.G.. Buonopane, Modeling the seismic response of cold-formed steel framed buildings: Model development for the CFS-NEES building, Struct. Stab. Res. Counc. Annu. Stab. Conf. 2013, SSRC 2013. (2013) 426–442. http://www.scopus.com/inward/record.url?eid=2-s2.0-84883374860&partnerID=40&md5=035e26ef0181ae5611c16d94776dd18b.

[4] M. Zeynalian, H.R. Ronagh, Seismic performance of cold formed steel walls sheathed by fibre-cement board panels, J. Constr. Steel Res. 107 (2015) 1–11. doi:10.1016/j.jcsr.2015.01.003.

[5] O. Iuorio, V. Macillo, M.T. Terracciano, T. Pali, L. Fiorino, R. Landolfo, Seismic response of Cfs strap-braced stud walls: Experimental investigation, Thin-Walled Struct. 85 (2014) 466–480. doi:10.1016/j.tws.2014.09.008.

[6] K.. Chung, L. Lau, Experimental investigation on bolted moment connections among cold formed steel members, Eng. Struct. 21 (1999) 898–911. doi:10.1016/S0141-0296(98)00043-1.

[7] M.F. Wong, K.F. Chung, Structural behaviour of bolted moment connections in cold-formed steel beam-column, 58 (2002) 253–274. doi:10.1016/S0143-974X(01)00044-X.

[8] J.B.P. Lim, D.A. Nethercot, Ultimate strength of bolted moment-connections between cold-formed steel members, Thin-Walled Struct. 41 (2003) 1019–1039. doi:10.1016/S0263-8231(03)00045-4.

[9] D. Dubina, A. Stratan, Z. Nagy, Full - Scale tests on cold-formed steel pitched-roof portal frames with bolted joints, Adv. Steel Constr. 5 (2009) 175–194.

[10] X. Zhang, K.J.R. Rasmussen, H. Zhang, Experimental investigation of locally and distortionally buckled portal frames, J. Constr. Steel Res. 122 (2016) 571–583.

doi:10.1016/j.jcsr.2016.04.017.
[11] H.B. Blum, K.J.R. Rasmussen, Experimental and numerical study of connection effects in long-span cold-formed steel double channel portal frames, J. Constr. Steel Res. 155 (2019) 480–491. doi:10.1016/j.jcsr.2018.11.013.
[12] Ž. Bučmys, A. Daniūnas, J.P. Jaspart, J.F. Demonceau, A component method for cold-formed steel beam-to-column bolted gusset plate joints, Thin-Walled Struct. 123 (2018) 520–527. doi:10.1016/j.tws.2016.10.022.
[13] Rinchen, K.J.R. Rasmussen, Behaviour and modelling of connections in cold-formed steel single C-section portal frames, Thin-Walled Struct. 143 (2019) 106233. doi:10.1016/j.tws.2019.106233.
[14] A.B. Sabbagh, S. Torabian, Semi-rigid floor-to-wall connections using side-framed lightweight steel structures: Concept development, Thin-Walled Struct. 160 (2021) 107345. doi:10.1016/j.tws.2020.107345.
[15] J.B.P. Lim, G.J. Hancock, G. Charles Clifton, C.H. Pham, R. Das, DSM for ultimate strength of bolted moment-connections between cold-formed steel channel members, J. Constr. Steel Res. 117 (2016) 196–203. doi:10.1016/j.jcsr.2015.10.005.
[16] Rinchen, K.J.R. Rasmussen, H. Zhang, Design of cold-formed steel single C-section portal frames, J. Constr. Steel Res. 162 (2019) 105722. doi:10.1016/j.jcsr.2019.105722.
[17] D.T. Phan, S.M. Mojtabaei, I. Hajirasouliha, T.L. Lau, J.B.P. Lim, Design and Optimization of Cold-Formed Steel Sections in Bolted Moment Connections Considering Bimoment, J. Struct. Eng. 146 (2020) 04020153. doi:10.1061/(asce)st.1943-541x.0002715.
[18] S.M. Mojtabaei, J. Becque, I. Hajirasouliha, Local Buckling in Cold-Formed Steel Moment-Resisting Bolted Connections: Behavior, Capacity, and Design, J. Struct. Eng. 146 (2020) 04020167. doi:10.1061/(asce)st.1943-541x.0002730.

[19] S.M. Mojtabaei, J. Becque, I. Hajirasouliha, Behaviour and design of cold-formed steel bolted connections under combined actions, J. Struct. Eng. (2021) 04021013. doi:10.1061/(ASCE)ST.1943-541X.0002966.

[20] A.B. Sabbagh, M. Petkovski, K. Pilakoutas, R. Mirghaderi, Experimental work on cold-formed steel elements for earthquake resilient moment frame buildings, Eng. Struct. 42 (2012) 371–386. doi:10.1016/j.engstruct.2012.04.025.

[21] A.B. Sabbagh, M. Petkovski, K. Pilakoutas, R. Mirghaderi, Cyclic behaviour of bolted cold-formed steel moment connections: FE modelling including slip, J. Constr. Steel Res. 80 (2013) 100–108. doi:10.1016/j.jcsr.2012.09.010.

[22] CEN, Eurocode 3: Design of steel structures - Part 1-8: Design of joints, European Committee for Standardization, 2005.

[23] M.H. Serror, E.M. Hassan, S.A. Mourad, Experimental study on the rotation capacity of cold-formed steel beams, J. Constr. Steel Res. 121 (2016) 216–228. doi:10.1016/j.jcsr.2016.02.005.

[24] M. Shahini, A.B. Sabbagh, P. Davidson, R. Mirghaderi, Cold-formed steel bolted moment-resisting connections with friction-slip mechanism for seismic areas, Wei-Wen Yu Int. Spec. Conf. Cold-Formed Steel Struct. 2018 - Recent Res. Dev. Cold-Formed Steel Des. Constr. (2018) 389–395.

[25] J. Ye, More efficient cold-formed steel elements and bolted connections, PhD Thesis, The University of Sheffield, 2016.

[26] J. Ye, S.M. Mojtabaei, I. Hajirasouliha, Seismic performance of cold-formed steel bolted moment connections with bolting friction-slip mechanism, J. Constr. Steel Res. 156 (2019) 122–136. doi:10.1016/j.jcsr.2019.01.013.

[27] S.M. Mojtabaei, I. Hajirasouliha, J. Ye, Optimisation of cold-formed steel beams for best seismic performance in bolted moment connections, J. Constr. Steel Res. 181 (2021)

106621. doi:10.1016/j.jcsr.2021.106621.

[28] Dassault Systèmes Simulia, Abaqus 6.14 CAE User Guide, 2014.

[29] A.B. Sabbagh, Cold - Formed Steel Elements for Earthquake Resistant Moment Frame Buildings, PhD Thesis, The University of Sheffield, 2011.

[30] J. Ye, S.M. Mojtabaei, I. Hajirasouliha, K. Pilakoutas, Efficient design of cold-formed steel bolted-moment connections for earthquake resistant frames, Thin-Walled Struct. (2019) 0–1. doi:10.1016/j.tws.2018.12.015.

[31] S.M. Mojtabaei, M.Z. Kabir, I. Hajirasouliha, M. Kargar, Analytical and experimental study on the seismic performance of cold-formed steel frames, J. Constr. Steel Res. 143 (2018) 18–31. doi:https://doi.org/10.1016/j.jcsr.2017.12.013.

[32] M.R. Haidarali, D.A. Nethercot, Finite element modelling of cold-formed steel beams under local buckling or combined local/distortional buckling, Thin-Walled Struct. 49 (2011) 1554–1562. doi:10.1016/j.tws.2011.08.003.

[33] W. Ramberg, W. Osgood, Description of stress-strain curves by three parameters - Technical Note No. 902, National Advisory Committee for Aeronautics, Washington, D.C., USA, 1943.

[34] N. Hill, Determination of stress-strain relations from the offset yield strength values. Technical Note No. 927, (1944).

[35] K.J.R. Rasmussen, Full-range stress–strain curves for stainless steel alloys, J. Constr. Steel Res. 59 (2003) 47–61.

[36] J. Ye, S.M. Mojtabaei, I. Hajirasouliha, Local-flexural interactive buckling of standard and optimised cold-formed steel columns, J. Constr. Steel Res. 144 (2018) 106–118. doi:10.1016/j.jcsr.2018.01.012.

[37] J. Ye, S.M. Mojtabaei, I. Hajirasouliha, P. Shepherd, K. Pilakoutas, Strength and deflection behaviour of cold-formed steel back-to-back channels, Eng. Struct. 177 (2018)

641–654. doi:10.1016/j.engstruct.2018.09.064.

[38] J.W. Fisher, On the behavior of fasteners and plates with holes, Lehigh University, Bethlehem, Pennsylvania, 1964.

[39] C. Uang, A. Sato, J. Hong, K. Wood, Cyclic testing and modeling of cold-formed steel special bolted moment frame connections, J. Struct. Eng. 136 (2010) 953–960. doi:10.1061/(ASCE)ST.1943-541X.0000190.

[40] B.. Schafer, T. Peköz, Computational modeling of cold-formed steel: characterizing geometric imperfections and residual stresses, J. Constr. Steel Res. 47 (1998) 193–210. doi:10.1016/S0143-974X(98)00007-8.

[41] A.C. Walker, Design and Analysis of Cold-formed Sections, Halsted Press, 1975.

[42] Z. Li, B.W. Schafer, Buckling analysis of cold-formed steel members with general boundary conditions using CUFSM: Conventional and constrained finite strip methods, Proc. Twent. Int. Spec. Conf. Cold-Formed Steel Struct. (2010) 17–31. doi:10.1016/j.tws.2006.03.013.

[43] J. Becque, Local-overall interaction buckling of inelastic columns: A numerical study of the inelastic Van der Neut column, Thin-Walled Struct. 81 (2014) 101–107. doi:10.1016/j.tws.2013.07.010.

[44] AISC, Seismic Provisions for Structural Steel Buildings, ANSI/AISC 341-16, (2016).

[45] CEN, Eurocode 3: Design of steel structures - Part 1-1: General rules and rules for buildings, European Committee for Standardization, 2010.

[46] FEMA, FEMA-350 Recommended Seismic Design Criteria for New Steel Moment-Frame Buildings, in: Intergovernmental Panel on Climate Change (Ed.), Cambridge University Press, Cambridge, 2000. https://www.cambridge.org/core/product/identifier/CBO9781107415324A009/type/book_part.

[47] Y. Shifferaw, B.W. Schafer, Inelastic bending capacity of cold-formed steel members, J. Struct. Eng. 138 (2012) 468–480. doi:10.1061/(ASCE)ST.1943-541X.0000469.

[48] American Society for Testing and Materials (ASTM), Standard Test Methods for Cyclic (Reversed) Load Test for Shear Resistance of Framed Walls for Buildings. ASTM E2126, West Conshohocken, USA, 2007.

[49] A. Chopra, Dynamics of structures: Theory and applications to earthquake engineering, 2nd edition, Prentice Hall, 2001.

[50] Y. Liu, Z. Guo, X. Liu, R. Chicchi, B. Shahrooz, An innovative resilient rocking column with replaceable steel slit dampers: Experimental program on seismic performance, Eng. Struct. 183 (2019) 830–840. doi:10.1016/j.engstruct.2019.01.059.

Table 1 Material properties for tests A1 and B1

Test	Element	$\sigma_{0.2}$ (MPa)	f_u (MPa)
A1	Beam	313	479
	Gusset Plate	353	516
B1	Beam	322	479
	Gusset Plate	308	474

Table 2 Connection configurations and selected design variables

<table>
<tr><th colspan="4">Web-connected (W-C)</th></tr>
<tr><td>t_b=1 mm
t_g= t_b, 1.5t_b, 2t_b, 3t_b</td><td>t_b=2 mm
t_g= t_b, 1.5t_b, 2t_b, 3t_b</td><td>t_b=4 mm
t_g= t_b, 1.5t_b, 2t_b, 3t_b</td><td>t_b=6 mm
t_g= t_b, 1.5t_b, 2t_b, 3t_b</td></tr>
<tr><td colspan="4">T-shape 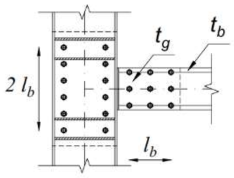 Rounded T-shape 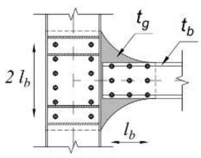 Chamfered shape 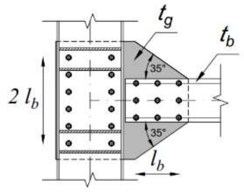</td></tr>
<tr><th colspan="4">Flange-connected (F-C)</th></tr>
<tr><td>t_b=1 mm
t_g= t_b, 2t_b, 3t_b, 4t_b, 5t_b, 6t_b</td><td>t_b=2 mm
t_g= t_b, 2t_b, 3t_b, 4t_b, 5t_b, 6t_b</td><td>t_b=4 mm
t_g= t_b, 2t_b, 3t_b</td><td>t_b=6 mm
t_g= t_b, 2t_b, 3t_b</td></tr>
<tr><td colspan="4">Unstiffened top and seat angles 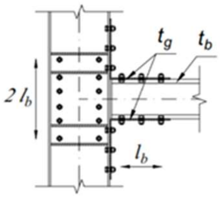 Stiffened top and seat angles 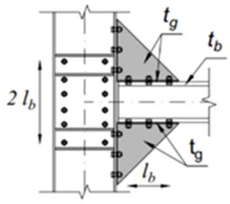</td></tr>
<tr><th colspan="4">Web and flange-connected (WF-C)</th></tr>
<tr><td>t_b=1 mm</td><td>t_b=2 mm</td><td>t_b=4 mm</td><td>t_b=6 mm</td></tr>
<tr><td>t_g= t_b, 1.5t_b, 2t_b, 3t_b</td><td>t_g= t_b, 1.5t_b, 2t_b, 3t_b</td><td>t_g= t_b, 1.5t_b, 2t_b, 3t_b</td><td>t_g= t_b, 1.5t_b, 2t_b, 3t_b</td></tr>
<tr><td colspan="4">T-shaped gusset plate and unstiffened top and seat angles 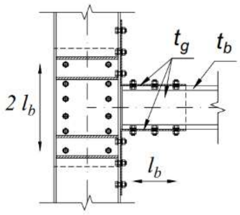</td></tr>
</table>

Table 3 Critical elastic stresses for local and distortional buckling for each beam type

Beam	$\sigma_{,l}$ (MPa)	$\sigma_{,d}$ (MPa)
tb=1 mm	92.10	128.83
tb=2 mm	364.74	272.33
tb=4 mm	-	609.16
tb=6 mm	-	1013.56

Table 4. 3D graphical representations of different connection types

Web-connected (W-C)		
T-shape	Rounded T-shape	Chamfered shape
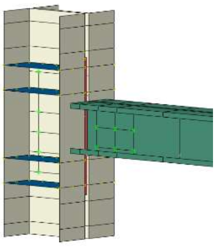	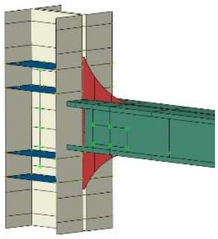	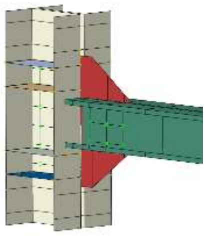
Flange-connected (F-C)		
Unstiffened top and seat angles	Stiffened top and seat angles	
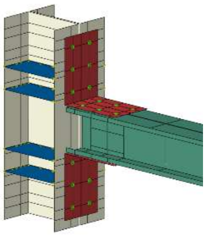	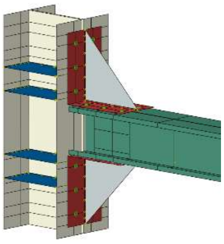	
Web and flange-connected (WF-C)		
T-shaped gusset plate and unstiffened top and seat angles		
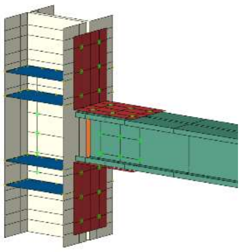		

Table 5 Ultimate rotation (ϕ_{max}), flexural rigidity per EC3 [22], rotational category per AISC provisions [44] and failure modes of W-C connections

Beam thickness t_b	Gusset plate thickness t_g	T-shape				Rounded T-shape				Chamfered shape			
		Failure mode	EC3 rotational rigidity	ϕ_{max} (rad)	AISC category	Failure mode	EC3 rotational rigidity	ϕ_{max} (rad)	AISC category	Failure mode	EC3 rotational rigidity	ϕ_{max} (rad)	AISC category
1 mm	t_b	GP	S-R	0.01	OMF	GP	S-R	0.006	OMF	GP	S-R	0.01	OMF
	$1.5t_b$	GP	S-R	0.011	OMF	GP	S-R	0.01	OMF	B	R	0.025	IMF
	$2t_b$	GP	S-R	0.013	OMF	B	S-R	0.024	IMF	B	R	0.035	IMF
	$3t_b$	GP	S-R	0.017	OMF	B	R	0.032	IMF	B	R	0.03	IMF
2 mm	t_b	GP	S-R	0.013	OMF	GP	S-R	0.012	OMF	GP	S-R	0.014	OMF
	$1.5t_b$	GP	S-R	0.016	OMF	GP	S-R	0.02	OMF	B	R	0.023	IMF
	$2t_b$	GP	S-R	0.021	IMF	B	S-R	0.023	IMF	B	R	0.022	IMF
	$3t_b$	GP	S-R	0.059	SMF	B	R	0.022	IMF	B	R	0.022	IMF
4 mm	t_b	GP	S-R	0.025	IMF	GP	S-R	0.027	IMF	GP	S-R	0.028	IMF
	$1.5t_b$	GP	S-R	0.05	SMF	GP	S-R	0.06	SMF	B	S-R	0.06	SMF
	$2t_b$	GP	S-R	0.06	SMF	B	S-R	0.06	SMF	B	R	0.06	SMF
	$3t_b$	GP	S-R	0.056	SMF	B	S-R	0.06	SMF	B	R	0.06	SMF
6 mm	t_b	GP	S-R	0.048	SMF	GP	S-R	0.06	SMF	GP	S-R	0.052	SMF
	$1.5t_b$	GP	S-R	0.06	SMF	GP	S-R	0.06	SMF	GP	S-R	0.06	SMF
	$2t_b$	GP	S-R	0.056	SMF	GP	S-R	0.06	SMF	B	S-R	0.06	SMF
	$3t_b$	GP	S-R	0.06	SMF	B	S-R	0.06	SMF	B	S-R	0.06	SMF

(GP): Gusset plate failure, (B): Beam failure

Table 6 Ultimate rotation (ϕ_{max}), flexural rigidity per EC3 [22], rotational category per AISC provisions [44] and failure modes of F-C connections

Beam thickness t_b	Gusset plate thickness t_g	Unstiffened top and seat angles				Stiffened top and seat angles			
		Failure mode	EC3 rotational rigidity	ϕ_{max} (rad)	AISC category	Failure mode	EC3 rotational rigidity	ϕ_{max} (rad)	AISC category
1 mm	t_b	A	P	0.06	SMF	A	P	0.06	SMF
	$2t_b$	A	P	0.06	SMF	A	P	0.06	SMF
	$3t_b$	A	P	0.06	SMF	B	S-R	0.06	SMF
	$4t_b$	A	P	0.06	SMF	B	S-R	0.06	SMF
	$5t_b$	A	S-R	0.06	SMF	B	S-R	0.038	IMF
	$6t_b$	A	S-R	0.06	SMF	B	S-R	0.025	IMF
2 mm	t_b	A	P	0.06	SMF	A	P	0.06	SMF
	$2t_b$	A	P	0.06	SMF	A	S-R	0.06	SMF
	$3t_b$	A	P	0.06	SMF	B	S-R	0.06	SMF
	$4t_b$	A	S-R	0.06	SMF	B	S-R	0.055	SMF
	$5t_b$	A	S-R	0.06	SMF	B	S-R	0.029	IMF
	$6t_b$	A	S-R	0.06	SMF	B	S-R	0.023	IMF
4 mm	t_b	A	P	0.06	SMF	A	P	0.06	SMF
	$2t_b$	A	P	0.06	SMF	A	S-R	0.06	SMF

	$3t_b$	A	S-R	0.06	SMF	B	S-R	0.06	SMF
6 mm	t_b	A	S-R	0.06	SMF	A	S-R	0.06	SMF
	$2t_b$	A	S-R	0.06	SMF	A	S-R	0.06	SMF
	$3t_b$	A	S-R	0.06	SMF	B	S-R	0.06	SMF

(A): Stiffening plate and angle failure, (B): Beam failure

Table 7 Maximum rotation (ϕ_{max}), flexural rigidity as per EC3 [22], rotational category as per AISC provisions [44] and failure modes for WF-C connections

Beam thickness t_b	Gusset plate thickness t_g	T-shape with unstiffened top and seat angles			
		Failure mode	EC3 rotational rigidity	ϕ_{max} (rad)	AISC category
1 mm	t_b	GP	S-R	0.031	IMF
	$1.5t_b$	GP	S-R	0.032	IMF
	$2t_b$	GP	S-R	0.033	IMF
	$3t_b$	B	S-R	0.013	OMF
2 mm	t_b	GP	S-R	0.048	SMF
	$1.5t_b$	GP	S-R	0.06	SMF
	$2t_b$	GP	S-R	0.06	SMF
	$3t_b$	B	S-R	0.0215	IMF
4 mm	t_b	GP	S-R	0.06	SMF
	$1.5t_b$	GP	S-R	0.06	SMF
	$2t_b$	GP	S-R	0.06	SMF
	$3t_b$	B	S-R	0.037	IMF
6 mm	t_b	GP	S-R	0.06	SMF
	$1.5t_b$	GP	S-R	0.06	SMF
	$2t_b$	GP	S-R	0.06	SMF
	$3t_b$	B	S-R	0.06	SMF

(GP): Gusset plate and/or angle failure, (B): Beam failure

Table 8 Connections with balanced performance

Connection type	**EC3 beam class**	**Gusset plate thickness t_g**	**Failure mode**	**Gusset plate shape**
W-C	1, 2, 3 and 4	$2t_b$	B	Rounded T-shape
F-C	3 and 4	$4t_b$	B	Stiffened top and seat angles
	2	$3t_b$	B	
	1	$2t_b$	A	
WF-C	1, 2, 3 and 4	$2t_b$	GP	T-shape and unstiffened top and seat angles

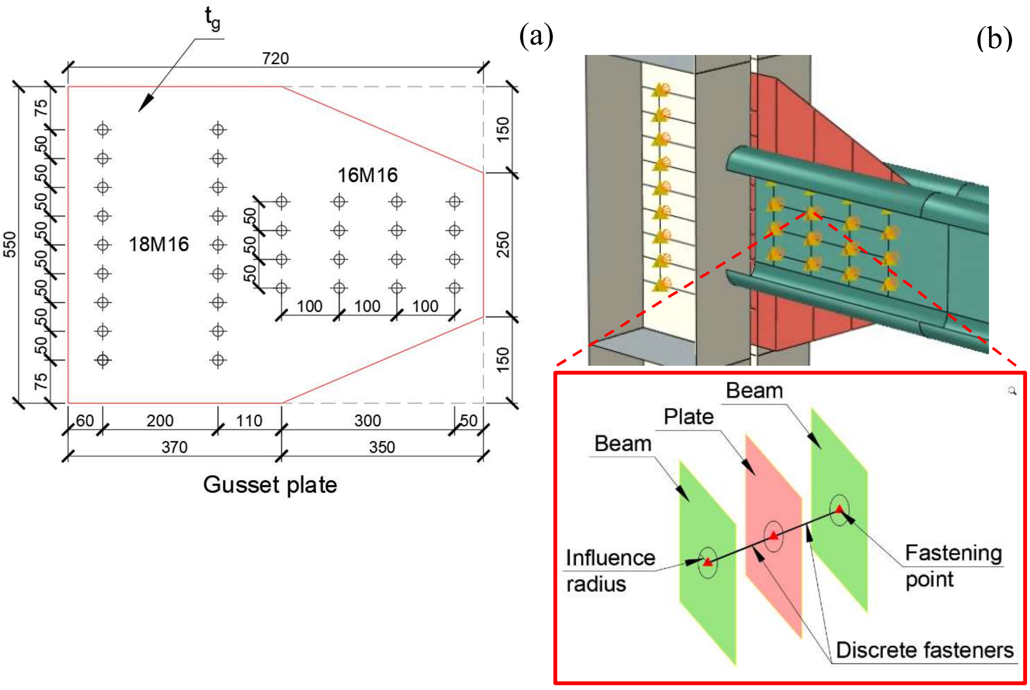

Fig. 1 FE modelling of the tested connections: a) bolt arrangement and b) discrete fasteners

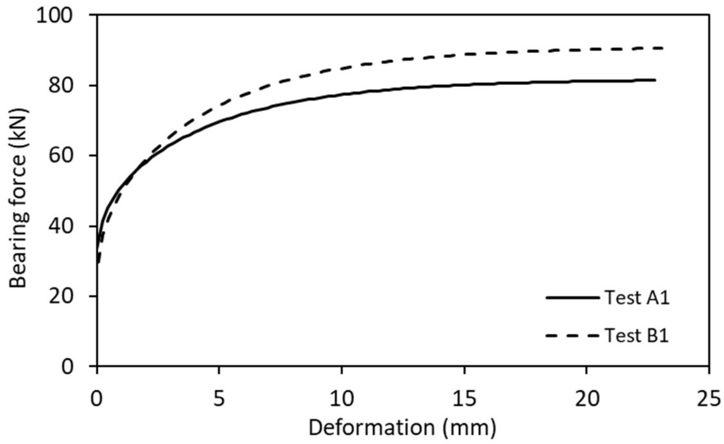

Fig. 2 Bearing behaviour of the beam to gusset plate bolts incorporated into the FE models of tests A1 and B1

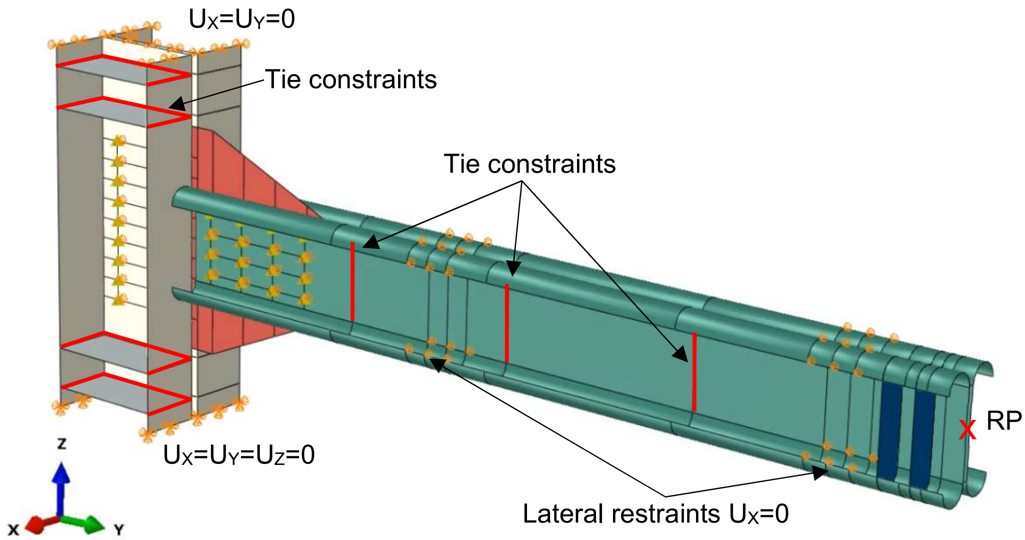

Fig. 3 Boundary conditions of the FE models

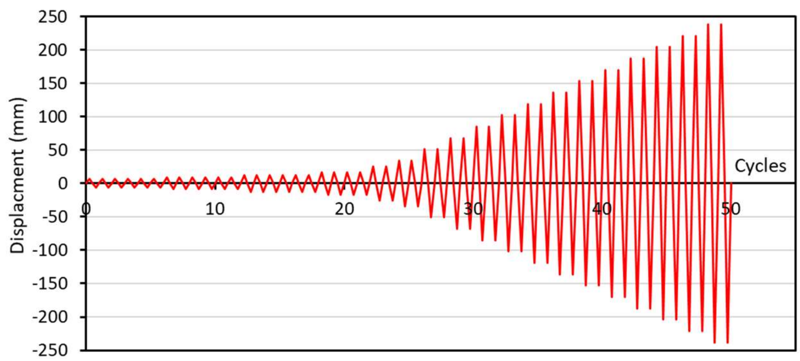

Fig. 4 Cyclic loading protocol adopted from AISC 341-16 [44]

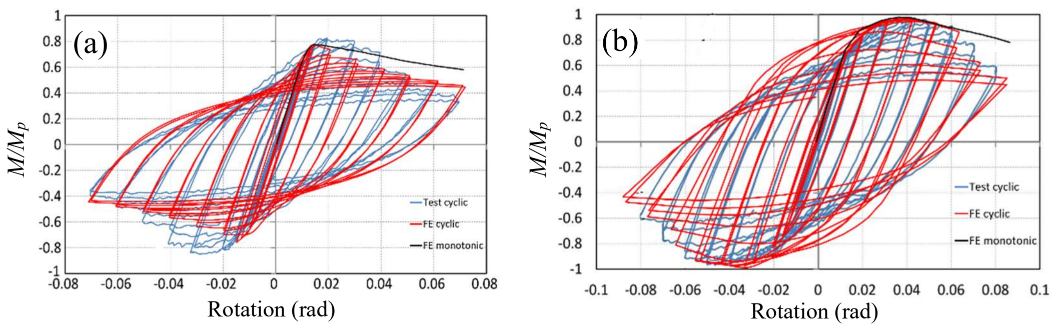

Fig. 5 Comparison between experimental moment-rotation behaviour [29] and FE analysis results for: (a) A1 and (b) B1 specimens

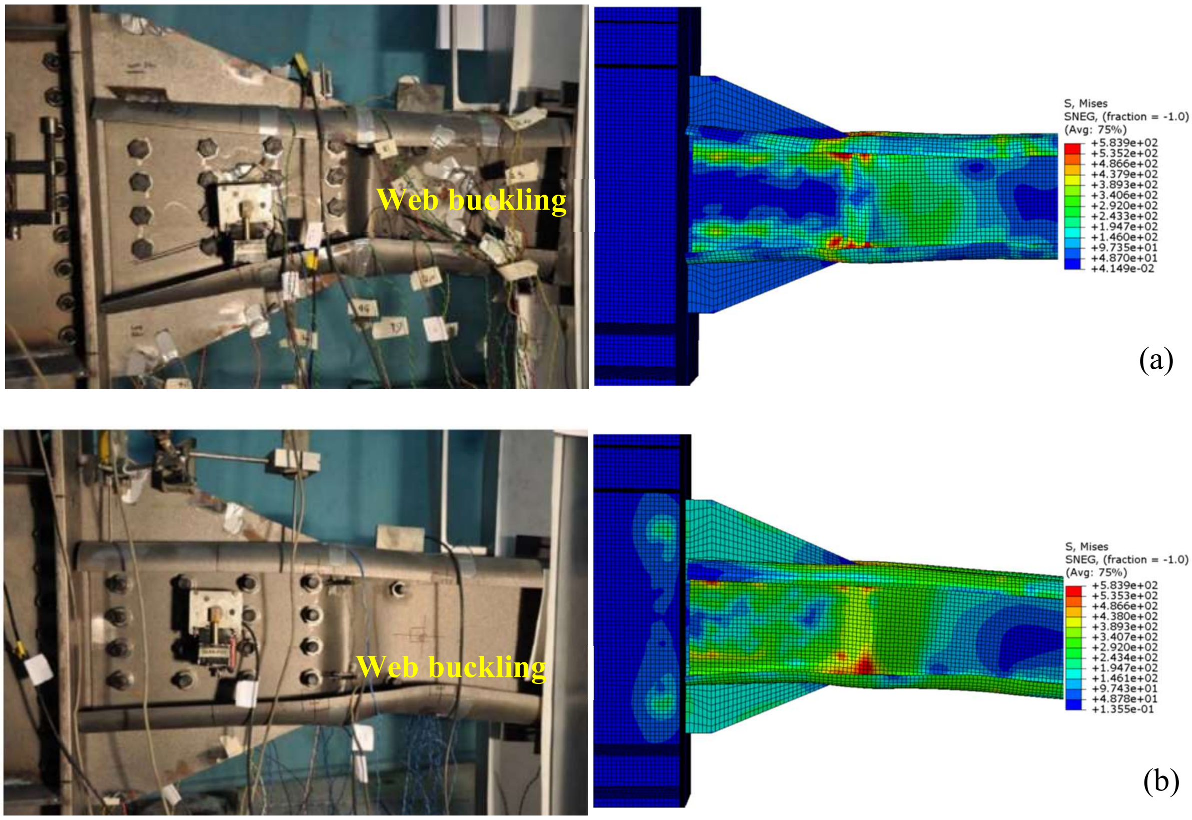

Fig. 6 Comparison between the experimental [29] and predicted failure modes under cyclic loading for: (a) A1 and (b) B1 specimens

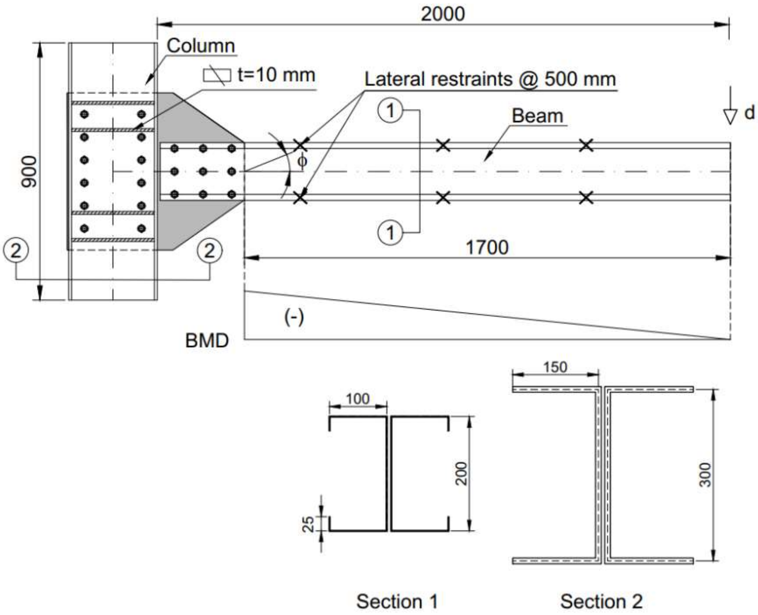

Fig. 7 Connection configuration

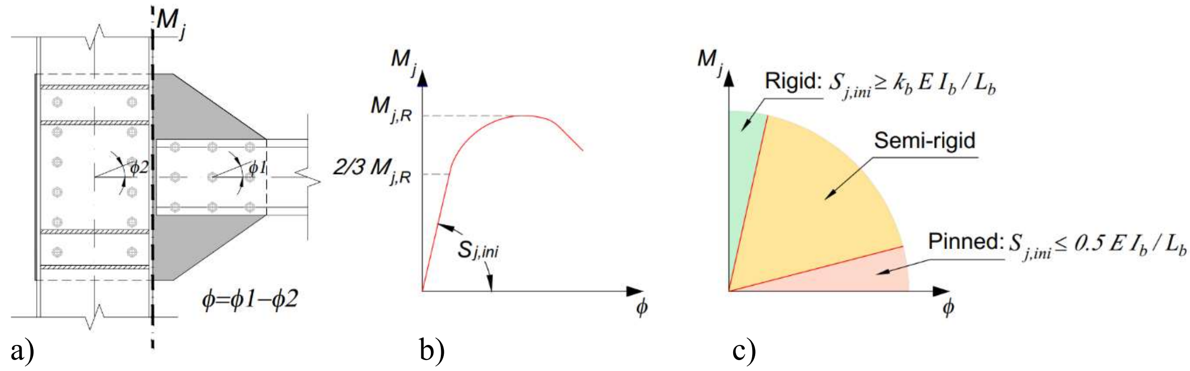

Fig. 8 Definition of a) moment-rotation relationship, b) initial stiffness ($S_{j,ini}$), and c) boundaries for the rotational stiffness classification of connections

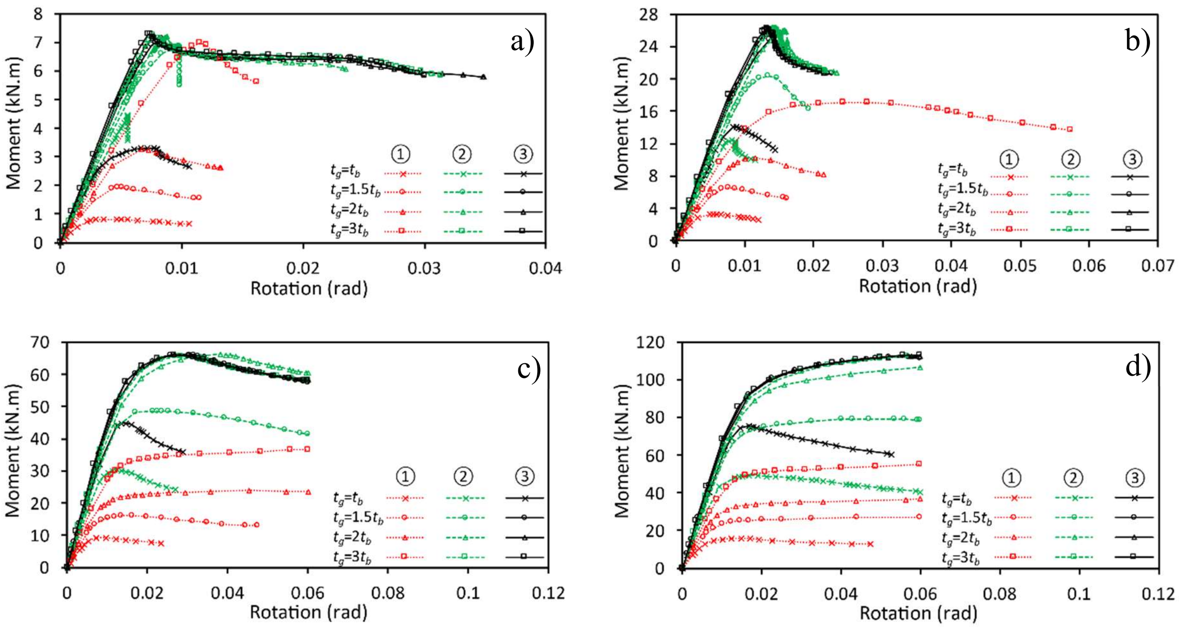

Fig. 9 Moment-rotation responses of W-C connections with various gusset plate thicknesses (t_g) and shapes (①: T-shape, ②: rounded T-shape and ③ chamfered shape), and beam thicknesses (t_b) of a) 1 mm, b) 2 mm, c) 4 mm and d) 6 mm

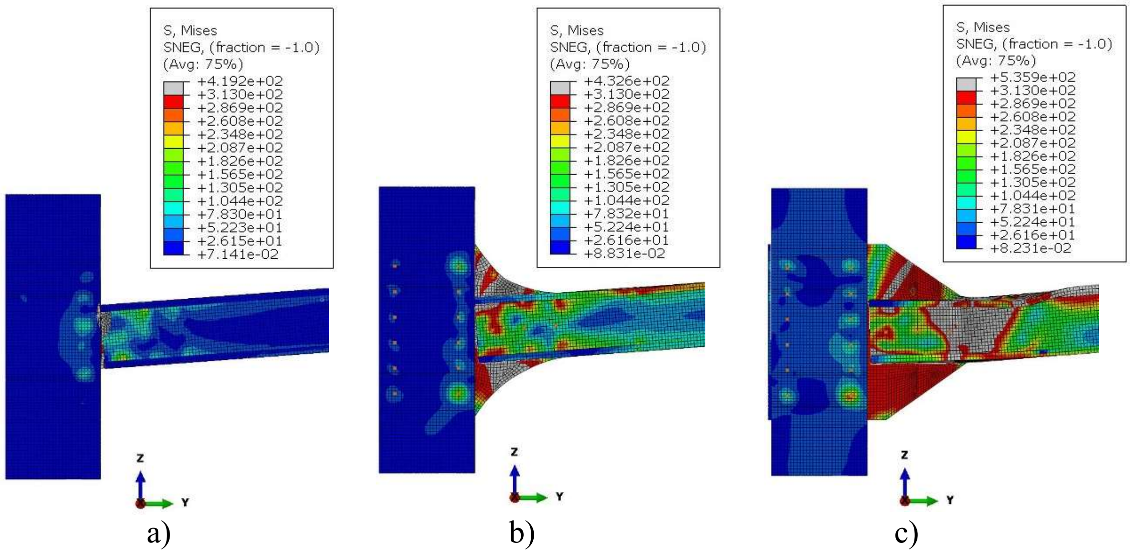

Fig. 10 Failure modes of W-C connections with: a) T shaped, b) rounded T-shaped and c) chamfered gusset plate, for t_b=4 mm and t_g=1.5t_b

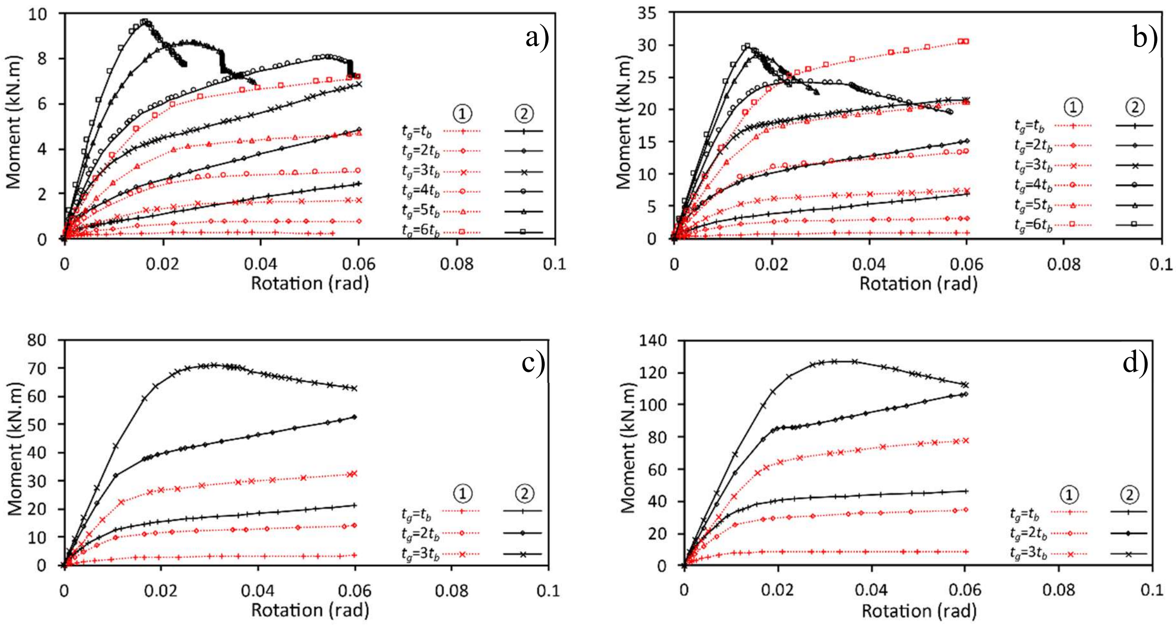

Fig. 11 Moment-rotation responses of F-C connections with various gusset plate thicknesses (t_g) and shapes (①: unstiffened angles and ②: stiffened angles), and beam thicknesses (t_b) of a) 1 mm, b) 2 mm, c) 4 mm and d) 6 mm

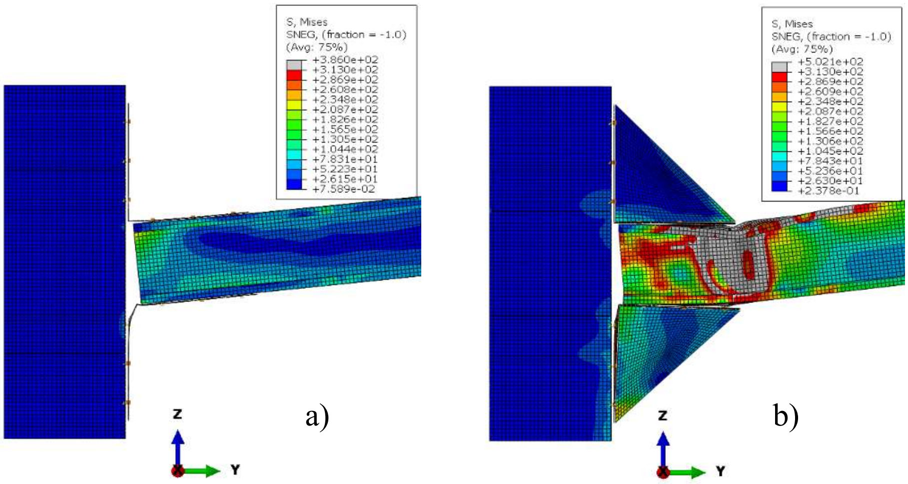

Fig. 12 Failure modes of connections with a) unstiffened angles and b) stiffened angles, when t_b=2 mm and t_g=3t_b

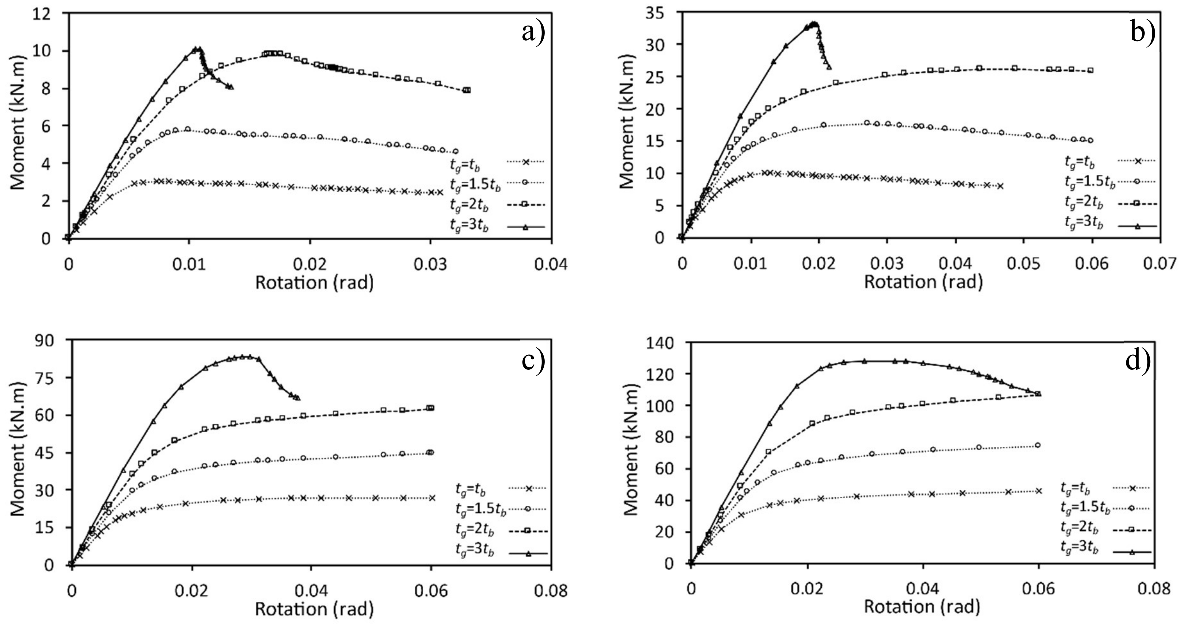

Fig. 13 Moment-rotation responses of WF-C connections with various gusset plate and angle thicknesses (t_g), and beam thicknesses (t_b) of a) 1 mm, b) 2 mm, c) 4 mm and d) 6 mm

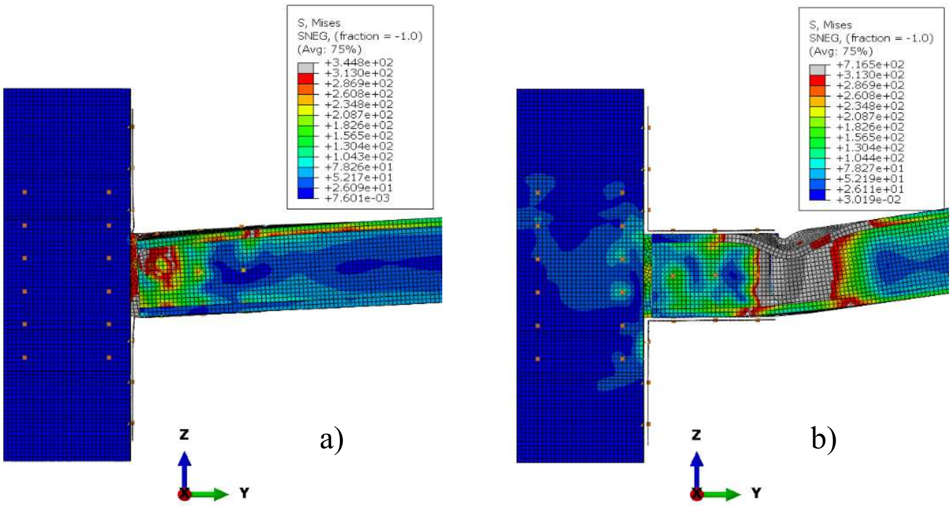

Fig. 14 Failure modes of WF-C connections for t_b=1 mm and a) t_g=t_b and b) t_b=3t_b

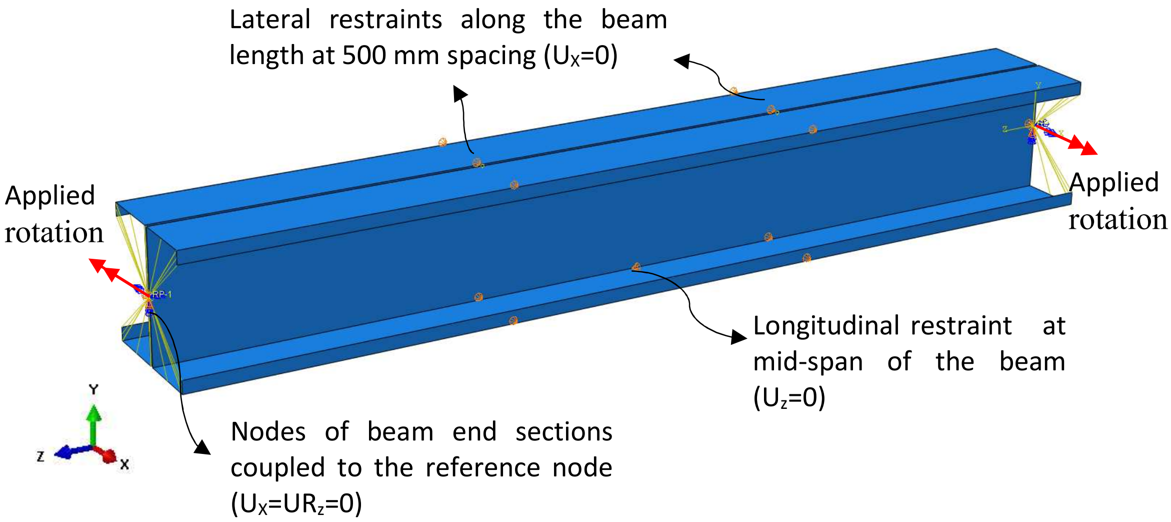

Fig. 15 FE model of CFS beam with back-to-back channel sections used to determine the cross-sectional flexural capacity ($M_{u,b}$)

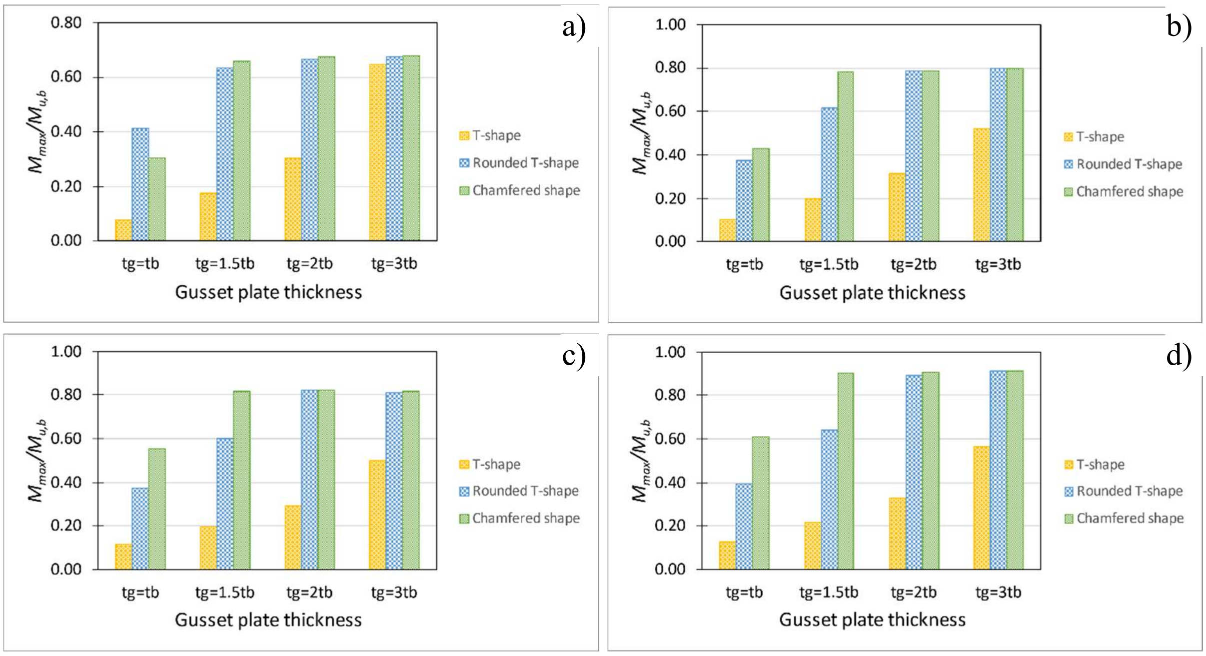

Fig. 16 $M_{max}/M_{u,b}$ ratios for W-C connections with beam thicknesses t_b of a) 1 mm, b) 2 mm, c) 4 mm and d) 6 mm

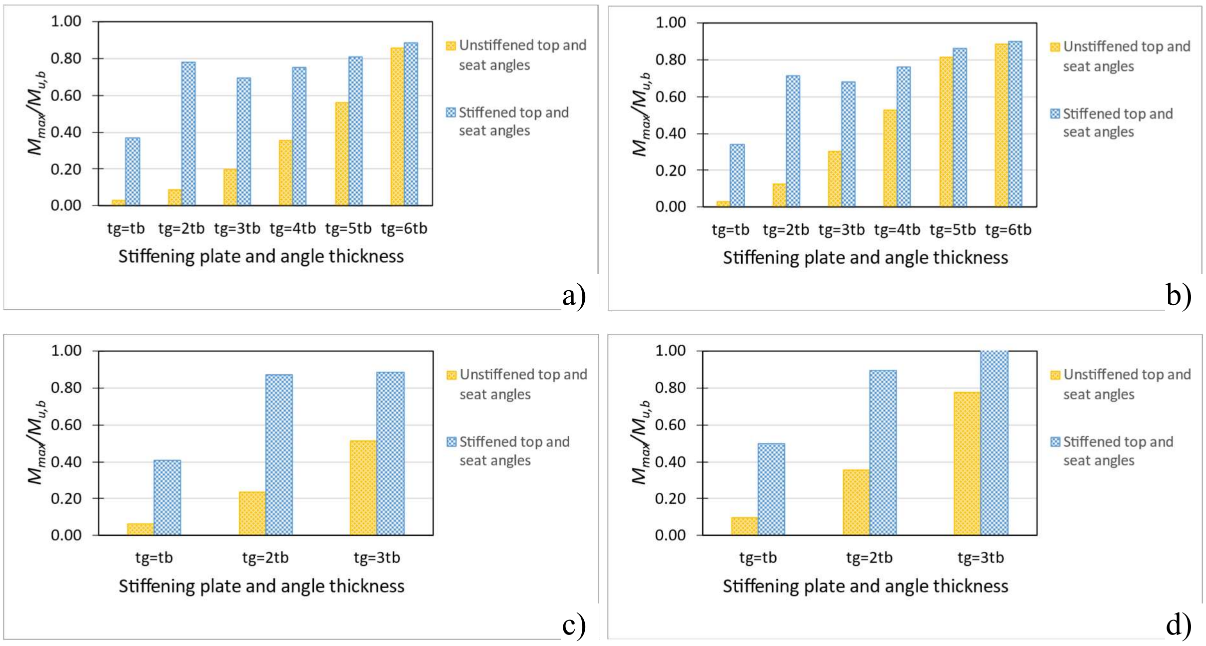

Fig. 17 $M_{max}/M_{u,b}$ ratios for F-C connections with beam thicknesses t_b of a) 1 mm, b) 2 mm, c) 4 mm and d) 6 mm

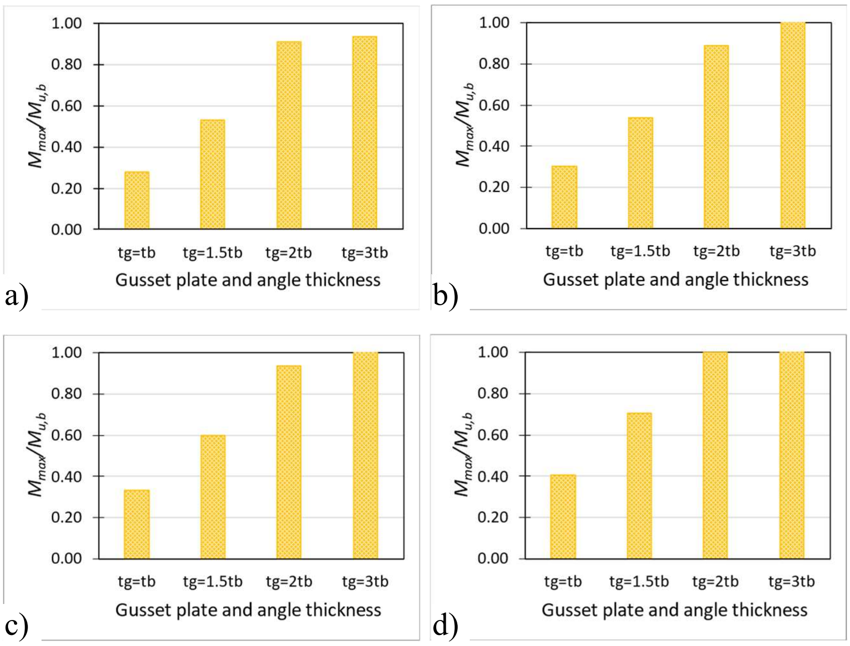

Fig. 18 M_{max}/M_{ub} ratios for WF-C connections with beam thicknesses t_b of a) 1 mm, b) 2 mm, c) 4 mm and d) 6 mm

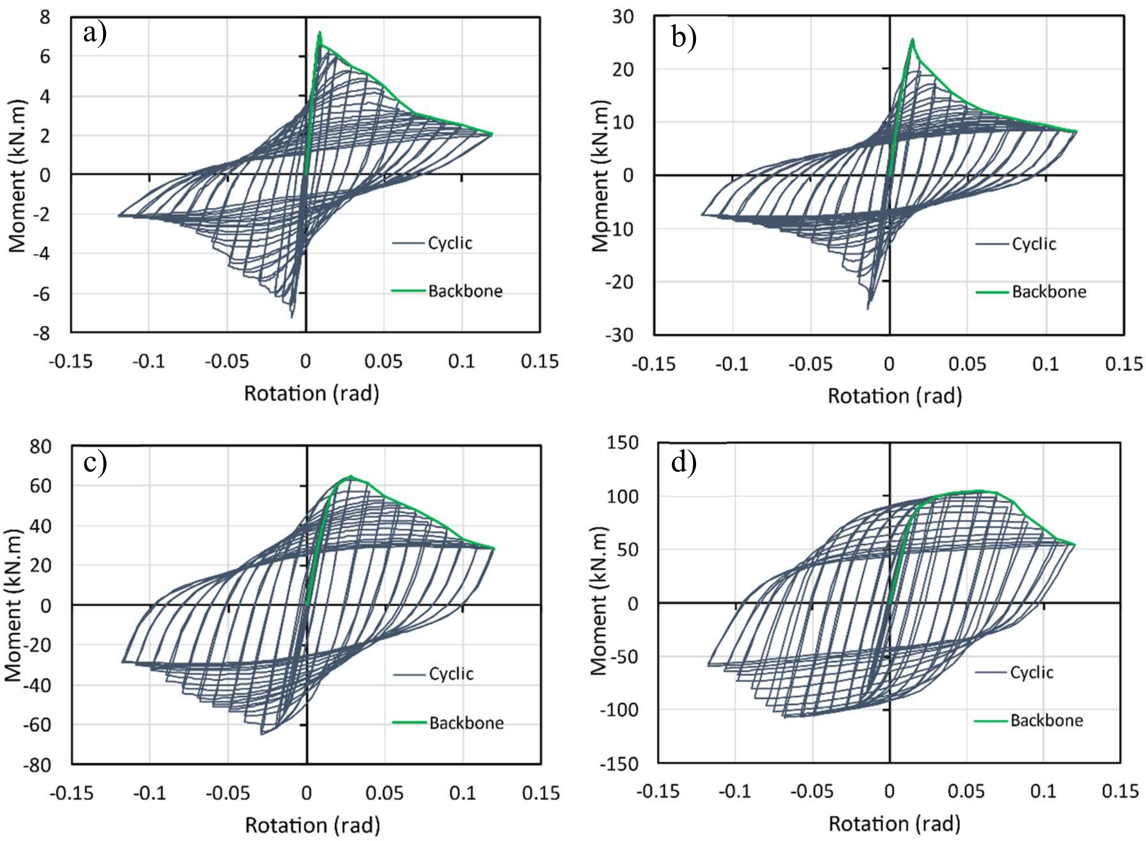

Fig. 19 Hysteretic moment-rotation curves for balanced W-C connections with gusset plate thickness $t_g=2t_b$ and beam thickness (t_b) of a) 1 mm, b) 2 mm, c) 4 mm and d) 6 mm

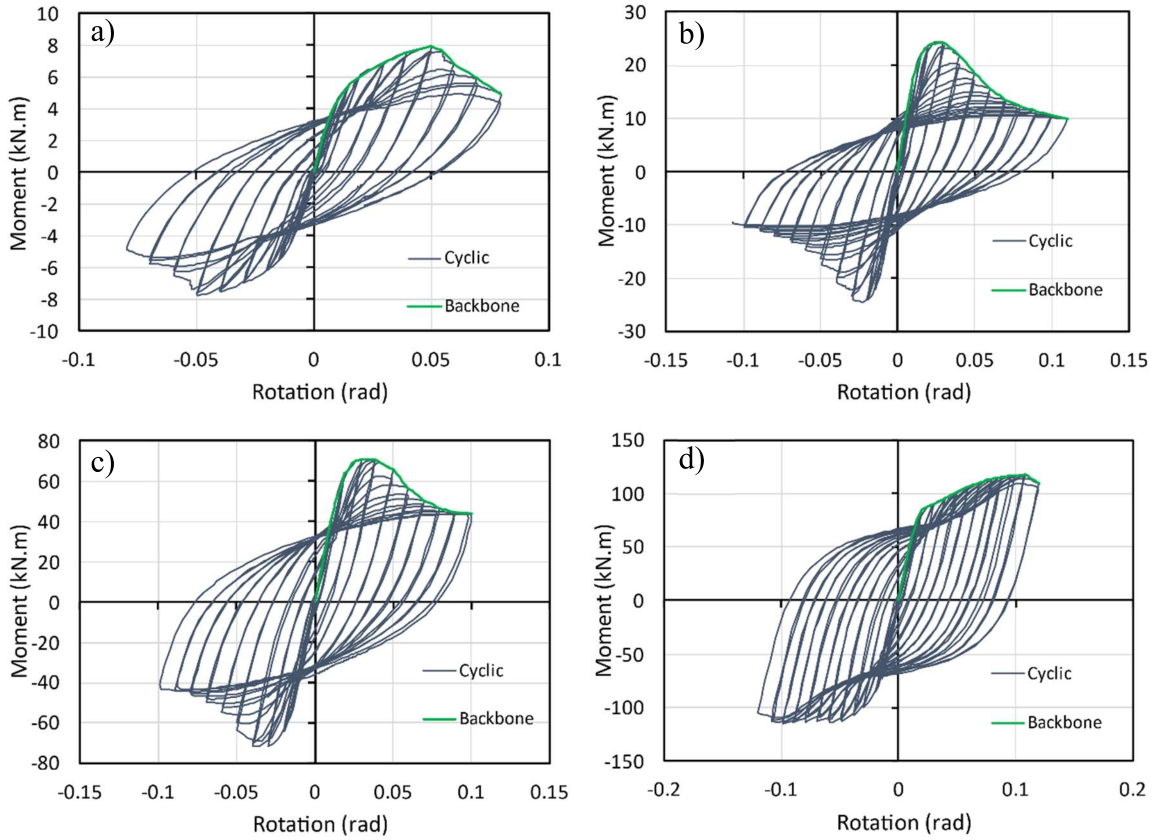

Fig. 20 Hysteretic moment-rotation curves for balanced F-C connections with beam and gusset plate thicknesses of a) t_b=1 mm, t_g=4t_b, b) t_b=2 mm, t_g=4t_b, c) t_b=4 mm, t_g=3t_b and d) t_b=6 mm, t_g=2t_b

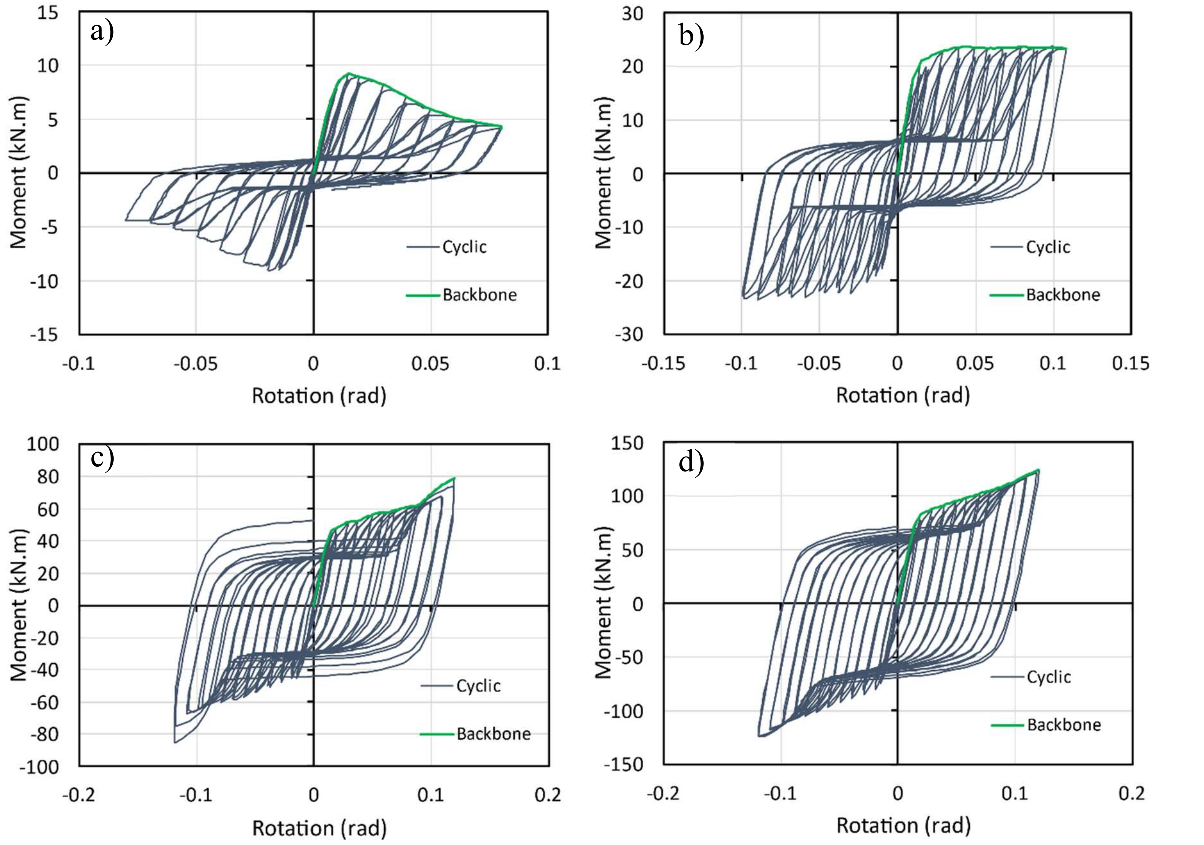

Fig. 21 Hysteretic moment-rotation curves for balanced WF-C connections with gusset plate thickness t_g=2t_b and beam thickness (t_b) of a) 1 mm, b) 2 mm, c) 4 mm and d) 6 mm

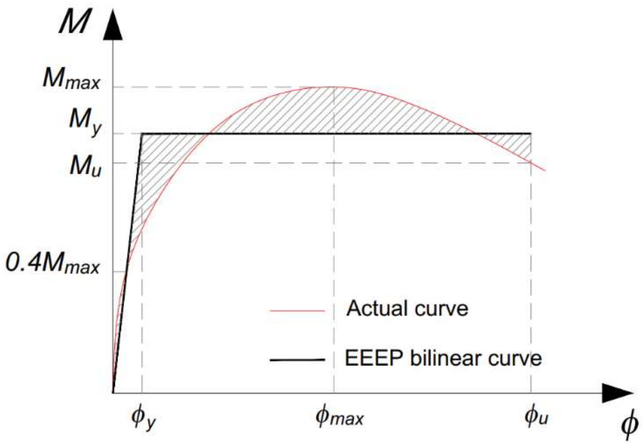

Fig. 22 Equivalent (EEEP) analysis model per ASTM E2126

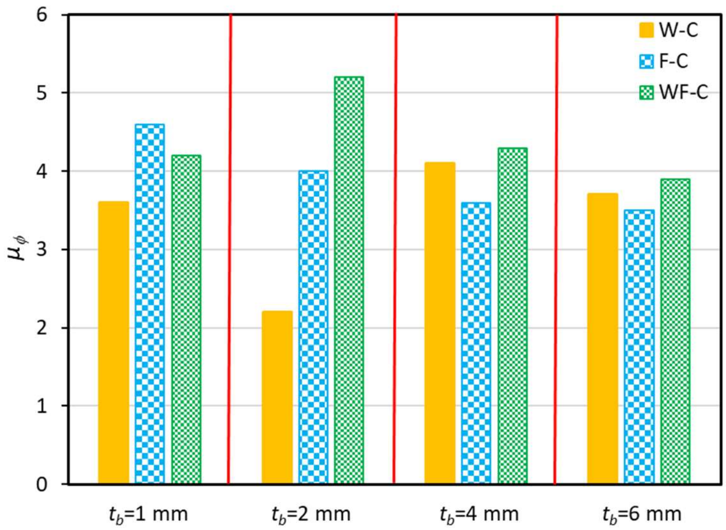

Fig. 23 Ductility (μ_ϕ) of different connection configurations with balanced performance

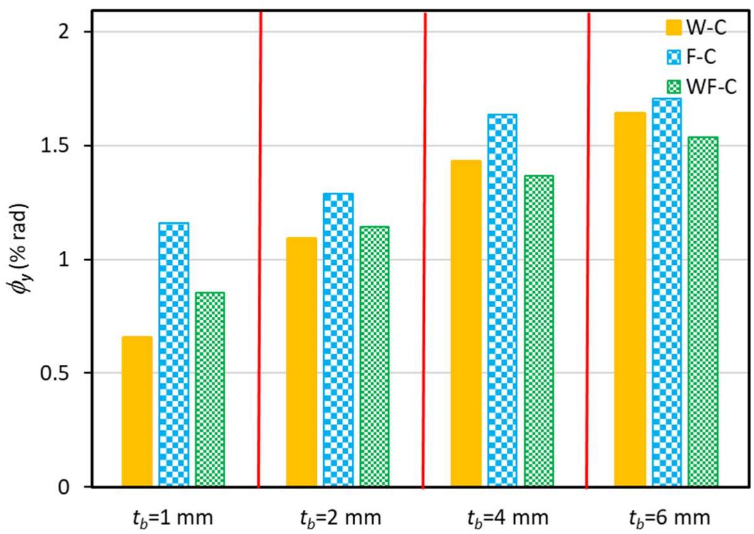

Fig. 24 Yield rotation *(ϕ_y)* of different connection configurations with balanced performance

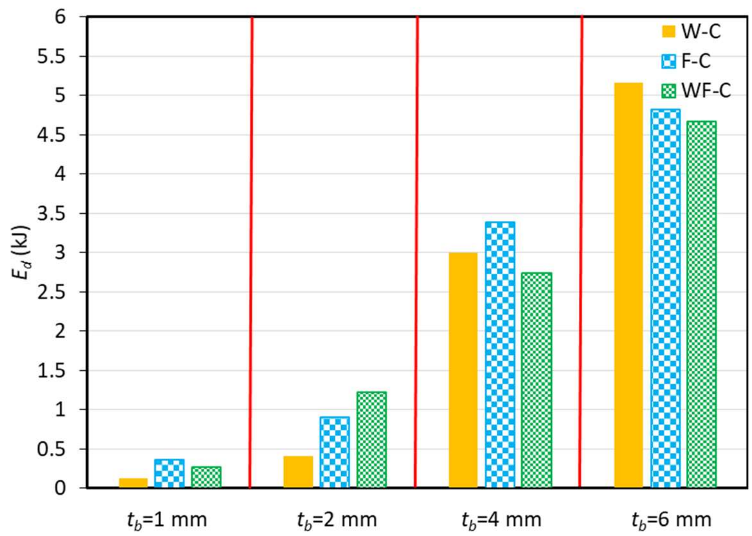

Fig. 25 Energy dissipation (E_d) of connections with balanced performance

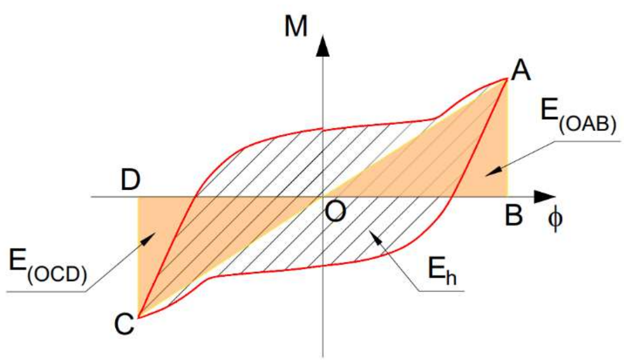

Fig. 26 Definition of equivalent viscous damping coefficient (ξ_{eq})

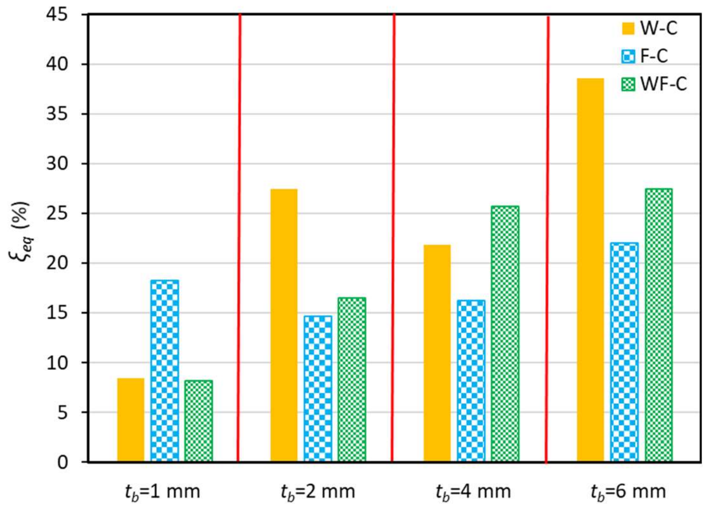

Fig. 27 Equivalent viscous damping coefficient (ξ_{eq}) at M_{max} for connections with balanced performance

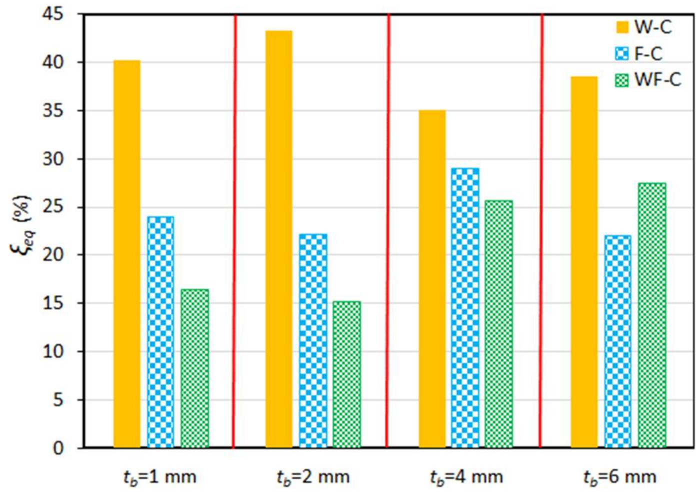

Fig. 28 Equivalent viscous damping coefficient (ξ_{eq}) at M_u for connections with balanced performance